Spring 2015

A Coplanar Edge-Fed Optically-Transparent Microstrip Patch Antenna Operating in the 5-6 GHz Frequency Spectrum

Eric Escobar
University of New Hampshire, Durham

Recommended Citation

Escobar, Eric, "A Coplanar Edge-Fed Optically-Transparent Microstrip Patch Antenna Operating in the 5-6 GHz Frequency Spectrum" (2015). *Master's Theses and Capstones*. 1020.
https://scholars.unh.edu/thesis/1020

A COPLANAR EDGE-FED OPTICALLY-TRANSPARENT MICROSTRIP PATCH ANTENNA OPERATING IN THE 5-6 GHZ FREQUENCY SPECTRUM

By

Eric Escobar
Bachelor of Science in Electrical Engineering, The University of New Hampshire, 2013

THESIS

Submitted to The University of New Hampshire
in Partial Fulfulllment of
the Requirements for the Degree of

Master of Science
in
Electrical Engineering

May, 2015

This thesis has been examined and approved in partial fulfillment of the requirements for the degree of Master of Science in Electrical Engineering by:

Thesis Director, Dr. Nicholas J. Kirsch, Assistant Professor of
Electrical and Computer Engineering

Dr. Kent A. Chamberlin, Professor of
Electrical and Computer Engineering

Dr. Michael J. Carter, Associate Professor of
Electrical and Computer Engineering

On April 23th, 2015

Original approval signatures are on file with The University of New Hampshire Graduate School.

Dedication

I would like to dedicate this thesis to my mom, Michele Escobar, and my two sisters, Sarah Escobar and Samantha Escobar.

I would also like to dedicate this thesis to my high school physics and chemistry teacher Mr. Roger Shelton for inspiring me to pursue a degree in an engineering field.

Acknowledgments

I would like to thank Dr. Nicholas Kirsch for advising me with the work associated with this thesis project. This opportunity provided me with the ability to continue my education at the University of New Hampshire. Also special thanks to Mr. Brough Turner and Dr. George Kontopidis of netBlazr who are responsible for the creation of this project.

I would like to thank the other members of my committee, Dr. Kent Chamberlin and Dr. Michael Carter. Their enthusiasm for the course material was paramount for the enjoyment felt throughout this program, and they have shown me what it means to be an educator. I would also like to thank them for their impact and assistance on this thesis project.

I would also like to thank my fellow graduate students. Jon Tefft and Braden Blanchette from the wireless system lab, who assisted with experimental setups and discussion with results obtained, and Ben Brownell who assisted with machining parts in the machine shop. Lastly, thanks to my family and friends who supported me throughout my education.

Eric Escobar

Table of Contents

APPENDICES

List of Figures

List of Tables

Abstract

A COPLANAR EDGE-FED OPTICALLY-TRANSPARENT MICROSTRIP PATCH ANTENNA OPERATING IN THE 5-6 GHZ FREQUENCY SPECTRUM

By

Eric Escobar

The University of New Hampshire, May, 2015

As wireless communications infiltrates our daily lives, there is a growing need for unobtrusive antennas. Utilizing optically transparent and electrically conductive material for antenna fabrication satisfies this demand. Optically transparent antennas have infiltrated applications in wireless communications where it is desired to reduce an antenna's visual or spatial impact. Their use in automotive applications preserves car aesthetics, while their integration onto solar cells of small satellites reduces size and thus weight. This work presents the development of a coplanar edge-fed optically transparent microstrip patch antenna, composed of highly conductive thin mesh wires designed to operate in the 5 to 6 GHz band, to be used in a phased array for beamforming and beamsteering applications. A simulation-based analysis of two edge-fed feeding mechanisms showed an inset feed outperforms a quarter-wavelength impedance transformer under optically transparent mesh material design limitations. From the results of the simulation, an optically transparent microstrip patch antenna was fabricated, and its performance was shown to be comparable to an antenna composed of solid copper.

CHAPTER 1

Introduction

The ability to communicate through a wireless connection has been evolving and growing since Guglielmo Marconi demonstrated its ability to provide continuous contact with ships sailing the English channel in 1897 [1]. By 1901, just four years later, radio reception had been established across the Atlantic Ocean [2], and this rapid expansion has evolved into a wireless infrastructure which currently supports more than seven billion mobile devices [3]. According to Cisco's global mobile data forecast, nearly two billion mobile devices, of the seven billion, are Wi-Fi capable devices. Wireless network technologies have allowed for network extensions into areas where hard wiring would be expensive or difficult. These networks have become so commonplace that one doesn't think twice before checking social media on a laptop, or another Wi-Fi capable device, while at the local coffee shop.

Aside from convenience, wireless networks offer several benefits, with the largest being flexibility. Radio Frequency (RF) signals can penetrate walls and propagate over large distances, enabling users to maintain a connection while on the move; whether it be in the same room, or across multiple floors in the same building. Not only does a wireless network allow users to move freely about, they also can accommodate a large number of users in a given area, where it is not feasible to have the necessary hardware, cabling and switches to support everyone. Additionally, the costly cabling is removed, and with that, it makes it easier to expand the network. Users can be added quickly without worrying about how the new office space configuration will affect the network connections. This technology has allowed for various connections to be made all across the globe, and there are however various challenges associated with a wireless channel.

1.1 Challenges of Wireless Communications

The expectation of wireless communications performance is to be on par with a wired communication system. However, for a wireless system, there are more performance limiting factors. The distance over which a signal can be transmitted is limited by propagation losses as well as interference from nearby systems operating in the same frequency range [4]. To combat the propagation losses, increasing the transmit power of the system will increase its range, however there is still an issue of interference. Directional antennas however, can be used to mitigate interference as well as increase the distance over which the signal can be transmitted, and therefore addresses both performance limiting factors [4]. The reason for this is because a directional antenna focuses the radiated energy in a single, or multiple, specified direction(s), and therefore the signal strength in the particular direction(s) will increase, resulting in the system's range increasing. Additionally, interference is reduced with a directional antenna, because the antenna will only receive energy from the particular direction(s).

In addition to propagation losses and the interference of nearby systems, the geographical landscape, consisting of natural and man-made obstacles, surrounding the system will also limit the operating range. This brings about the challenge of determining where the antenna can be mounted. For the best performance, it is desired to mount antennas high relative to the surrounding terrain, and therefore mounting on a tower or the edge of a tall building is best. Since the size of the antenna is determined by the desired operating frequency, it is fixed, and therefore antennas can be physically large and very obtrusive. Attempts have been made to disguise the antennas with their surroundings in order to reduce the visual impact, as shown in Figure 1.1. More specifically, Figure 1.1a shows a cell phone tower disguised as a tree to blend in with the tree growth, and Figure 1.1b shows a cell phone antenna disguised to match the brick exterior of the building.

(a) Cell phone tower [5]

(b) Antenna disguised to match brick building [6]

Figure 1.1: Disguising cell phone antennas

As shown by these two examples, sometimes the visual impact is reduced and sometimes the disguise is not successful, as Figure 1.1a shows a tower protruding far above the nearby trees. However, aside from the visual impacts, additional complications can arise with mounting. It may not always be possible to construct a tower to mount antennas on, and mounting on a building, either on the roof or its side may not be permitted due to cost as well as safety. As a result of this, mounting on the inside of a window is a viable option. Traditional antennas, when composed of copper however, are very obtrusive, as they would block the window. This not only has detrimental effects on the building's aesthetics, but on the energy consumption as well. Since the natural light is blocked by the antenna, lights will be used in a higher capacity, resulting in a greater energy consumption. Fabricating an antenna from an optically transparent and electrically conductive material will improve the antenna's visual impact, and would not block the window.

Previous work has shown there are a few main materials used for achieving optical transparency for conductive elements: transparent conducting oxide (TCO), conductive polymers, and thin mesh wires. Transparent conducting oxides, including indium tin oxide and fluorine tin oxide, are conductive materials that require advanced manufacturing and have sheet resistances near 4.6 Ω/sq. [7–9]. Conductive polymer antennas can be manufactured easily and are conformal, however they suffer from low conductivity as well as low optical transparency [10, 11]. More recently, highly conductive thin mesh wires were shown to have low sheet resistances, around 0.052 Ω/sq., and high optical transparency, 80.3%, [7, 12–16]. While transparent conducting oxides are less visible to the human eye than conductive meshes, their performance is inferior to conductive meshes due to intrinsic property limitations.

The use of optically transparent antennas extends beyond simply reducing an antenna's visual impact. This also allows for the antenna to be integrated into another section of the device which may have a positive consequence on the device's size. This is exemplified by [12], as they integrate a transparent antenna on a solar cell of a small satellite, and by [17], as they integrate a transparent antenna into an automobiles window or light panel.

1.2 Aim of this Research

The long term goal of this project is to facilitate the spread of high speed Internet connectivity to the un-served and underserved by creating neighborhood wireless networks which are adaptive, easily deployed, and have high capacity. Figure 1.2 compares the visual impact of an antenna node composed of solid copper and optically transparent material. These antennas are easily deployed by hanging them in the window. Not only is the optically transparent antenna easily deployed, but it is less obtrusive than the antenna composed of solid copper.

Figure 1.2: Compare visual impact of traditional and optically transparent antennas

The aim of this research was to show optically transparent material is a viable material to fabricate unobtrusive antennas. Prior work with optically transparent antennas utilized a probe-fed excitation, removing the optically transparent material from the feeding network. However, in this work the optically transparent material is used for the antenna as well as its feeding mechanism. Another objective of this research was to show optically transparent antenna elements can be deployed in a phased array for beamsteering and beamforming applications. The phased array emulates a directive antenna, which addresses performance limiting factors associated with wireless communications, while the optically transparent elements reduce the antenna's visual impact.

The contribution of this work is a simulation-based analysis investigating the challenges associated with direct contact coplanar feeding mechanisms and their performance. Next, optically transparent microstrip patch antennas were fabricated and their measured performance was compared to the performance of a solid copper antenna. Lastly, a simulation-based feasibility study was performed showing a uniform linear array (ULA) composed of dual-polarized optically transparent microstrip patch elements was capable of beamsteering applications.

This thesis is organized as follows:

- Chapter 2 presents related work and background information on material discussed in the thesis.
- Chapter 3 presents a simulation-based analysis on feeding techniques with optically transparent material limitations.
- Chapter 4 presents the procedure used to fabricate the antennas.
- Chapter 5 presents the empirical results measured with the fabricated antennas.
- Chapter 6 presents a simulation-based analysis on a dual polarized optically transparent antenna array.
- Chapter 7 presents a conclusion and future work.

CHAPTER 2

Background Information

This chapter presents background information on topics relevant to this thesis. The information will include concepts of radio frequency (RF) systems, prior work on conductive optically transparent materials, the theory of patch antennas, antenna arrays, and a description of the simulation and experiment test setup.

2.1 Radio Frequency (RF) Concepts

In this section, scattering parameters and skin depth are discussed. Scattering parameters are used to describe the performance of an RF system. For an antenna, the S-parameter measured is the S_{11} of the system, which is the reflection coefficient. This is a measure of how much energy is reflected back to the generator. This is important because a significant amount of energy reflected, means less energy is transmitted and the device is not efficient. Additionally, if the quantity of energy reflected back is too large, various components, such as amplifiers, can be damaged.

For RF signals, the current density in a conductor is non-uniform. It is highest at the conductors edge and exponentially drops off toward the center. A material's skin depth is a measure of the current density's exponential drop off. This is important for determining the thickness of a material to be used in an RF application.

2.1.1 Scattering Parameters

Scattering parameters are elements used to describe how radio frequency (RF) energy propagates through a multi-port network [19]. Equation 2.1 shows the scattering matrix for an N port network. For the S-parameter S_{ij} the j^{th} port is excited (input port) and the i^{th} port is the output port.

$$S = \begin{bmatrix} S_{11} & S_{12} & \cdots & S_{1N} \\ S_{21} & S_{22} & \cdots & S_{2N} \\ \vdots & \vdots & \ddots & \vdots \\ S_{N1} & S_{N2} & \cdots & S_{NN} \end{bmatrix} \tag{2.1}$$

The use of the scattering matrix allows complicated multi-port networks to be accurately described as simple "black boxes," with the individual scattering parameters describing an input-output path through the network for RF energy. When a RF signal is incident on a port, some of the energy is reflected back to that port, some of the energy can be transmitted to the other ports, and some of it is dissipated as heat or electromagnetic radiation [20]. Each S-parameter is complex because the network alters both the magnitude and phase of the input signal. However, the magnitude is typically of most interest to determine if connections are properly matched [20]. For a two-port network, the return loss (see Equation 2.2) and insertion loss (see Equation 2.3), expressed in decibels (dB), are the two quantities of interest [20].

$$\text{Return Loss} = -20\log|S_{11}| \tag{2.2}$$

$$\text{Insertion Loss} = -20\log|S_{21}| \tag{2.3}$$

A properly matched two port network has a high return loss and a low insertion loss, meaning there is minimal energy reflected and nearly all of the energy is transmitted.

2.1.2 Skin Depth

For direct current (DC), $f = 0$ Hz, the current density in a wire is uniform over the entire cross-sectional area of a conductor. This, however, is not true for alternating current (AC). Ampere's law from Maxwell's equations states that an electric current will induce a circulating magnetic field around any path that bounds the current [21, 22]. Since the current is changing with time, the induced magnetic field also changes with time. Faraday's law, from Maxwell's equations, states a changing magnetic field induces a circulating electric field [21, 22]. Therefore, with AC, eddy currents are induced which oppose the initial current flow. This effect is weak at the edges of a conductor and is stronger toward the center [20]. The result is a non-uniform current density which is highest at the edge of the conductor and exponentially drops off spatially. The current density distribution is described by the material's skin depth, which is a measure of the depth at which the current density reduces to $\sim$37% its initial value, and is a function of frequency f, permeability μ, and conductivity σ [20]. For a good conductor, ($\sigma \gg \omega\epsilon$) the skin depth can be calculated with Equation 2.4 [21, 23], where f is the frequency, μ is the material's permeability, and σ is the material's conductivity.

$$\delta_s \approx \frac{1}{\sqrt{\pi f \mu \sigma}} \tag{2.4}$$

The skin depth is very important when determining material thicknesses. At microwave frequencies, a material's resistance will be relatively constant for thicknesses greater than four skin depths ($t > 4\delta_s$). However, if the material's thickness is less than four skin depths, its resistance will dramatically increase [24]. This is because a conducting material of infinite thickness will have over 98% of the current flowing within a layer whose thickness is four skin depths [24].

2.2 Optically Transparent Materials

The ideal material for an optically transparent and electrically conducting element has the optical properties of glass and the electrical conductivity of copper or silver. There are various materials that are optically transparent and electrically conductive: transparent conducting oxides, transparent conducting polymers, and highly conductive thin wires in a mesh configuration (mesh material). The next three sections explain the characteristics of these materials.

2.2.1 Transparent Conducting Oxides (TCO)

Transparent conducting films composed of a transparent conducting oxides have been widely used in opto-electronic devices including liquid crystal displays, solar cells, and plasma displays [25, 26]. Recently these materials have been used for fabricating optically transparent antennas using various TCOs, such as ITO and FTO [7, 9, 17, 26–29]. The greatest advantage of a TCO such as ITO is its high optical transparency, as it is possible to achieve transparencies of up to 90% [7]. Figure 2.1 shows sheets of ITO material, and the high optical transparency can be qualitatively observed.

The optical transparency of a transparent conducting film largely depends on the thickness of the film deposition as well as the intrinsic material properties, specifically electron mobility and electron density [7, 8]. While increasing the electron mobility has a positive effect on both transparency and conductivity, increasing the electron density increases the

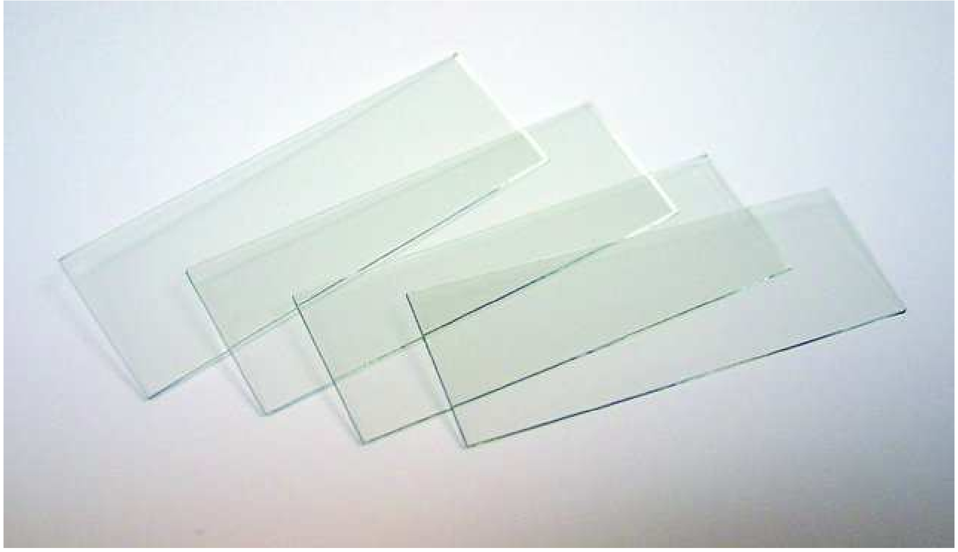

Figure 2.1: Sheets of ITO material [30]

electrical conductivity, but the optical transparency is sacrificed [8]. The high optical transparency is a strong advantage of the TCO materials. However, the high sheet resistance causes the efficiency to suffer [9]. Factors contributing to the sheet resistance are the same as those contributing to the optical transparency: film deposition thickness and intrinsic material properties [7]. The highest electron mobility available with the current technology provides a sheet resistance of 4.6 Ω/sq [7, 27]. While the conductivity of the material is a function of the material properties, skin-depth losses occur depending on film thickness, and the material's sheet resistance can dramatically increase if the film deposition thickness is less than four skin depths [8].

In addition to the already high sheet resistance of transparent conducting films, there is a significant increase in sheet resistance with humidity. In an environment with a relative humidity of 85%, studies show the sheet resistance of the TCO can increase by more than 150% within the short exposure time of ten hours, and an advanced fabrication procedure is required to produce films with a stable performance in humid conditions [28].

2.2.2 Transparent Conducting Polymers

Conducting polymers have become very promising material for flexible and printed electronics [31], and have been replacing TCO films in applications where low-temperature printable technology is needed [32]. The most popular and widely used polymer is Polystyrene Sulfonate (PEDOT-PSS) [33]. A major advantage of the conducting polymer material is its flexible nature. The PEDOT-PSS material can be integrated into moving structures as well as conform to non-flat surfaces [11]. In contrast to the flexibility, one disadvantage of a conducting polymer is the conductivity. Commercially available PEDOT-PSS has a low conductivity ($\sim$300 S/m), which is five orders of magnitude less than copper [11]. Studies have shown, however, that modifying the polymer with DMSO can increase the conductivity to be on par with TCOs [32]. The low conductivity results in a high sheet resistance. Nevrela *et al.* in [32] measured sheet resistances of 100 Ω/sq. This is dependent on the material thickness, which also affects the optical transparency of the element. Thin films can achieve optical transparencies of 70 to 80%, but they suffer from high losses due to the high sheet resistance [32]. As the film thickness is increased, the sheet resistance decreases. However, the optical transparency is severely degraded.

2.2.3 Mesh Material

The geometry of the optically transparent mesh material is shown in Figure 2.2, with the mesh line width, q, and pitch, p. The optical transparency can be increased or decreased by varying q and p. The optical transparency of the mesh material is quantitatively calculated by the percentage of non-mesh wire area to the total area of the material, as shown in

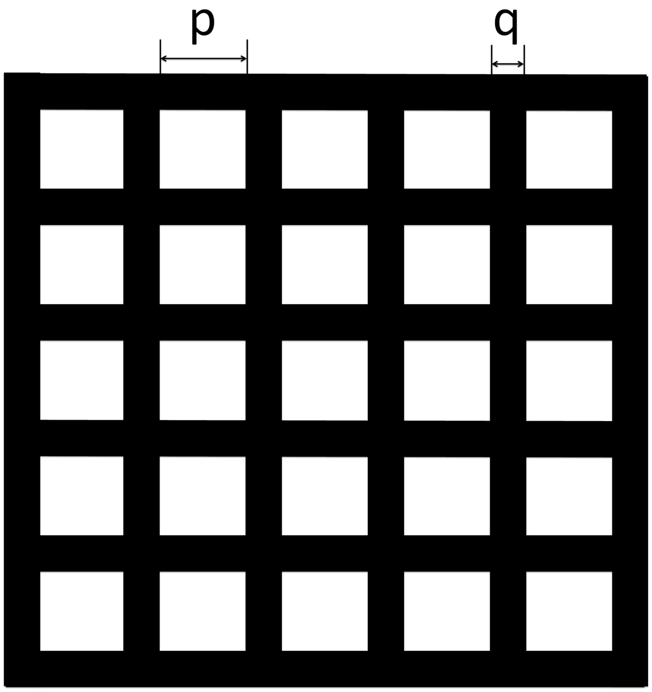

Figure 2.2: Optically transparent copper mesh material

Equation 2.5 [13].

$$\text{Optical Transparency} = \frac{A_{Non-Metal}}{A_{Total}} \cdot 100\% \tag{2.5}$$

For a rectangular cut of the mesh material with N rows and M columns of the mesh wires, the non-mesh wire area and total area of the rectangular cut are calculated with Equation 2.6 & 2.7 respectively.

$$A_{Non-Metal} = (M-1)(N-1)p^2 \tag{2.6}$$

$$A_{Total} = (N \cdot (q+p) - p)\,(M \cdot (q+p) - p) \tag{2.7}$$

Combining Equations 2.5 - 2.7, the optical transparency of the mesh material is calculated as a function of M and N, as well as q and p.

$$\text{Optical Transparency} = \frac{(M-1)(N-1)p^2}{(N{\cdot}(q+p)-p)\,(M{\cdot}(q+p)-p)}{\cdot}100\% \tag{2.8}$$

Though the optical transparency is greatly increased by increasing the pitch, p, of the mesh material, it brings with it the complication of limiting the realizable dimensions. As shown by Song *et al.* in [9], optimal performance is achieved with a continuous conductive strip along the edges of the patch antenna, and therefore only discrete dimensions which allow for the element to have a conductive strip along the edges should be used for good antenna performance. This is because in RF circuits, the current density is highest at the edges. Figure 2.3 shows a mesh grid with realizable dimensions as well as a mesh grid with non-realizable dimensions. Using the Equation 2.9, a realizable dimension D can be calculated, where q and p are the mesh line width and pitch respectively, and the total number of mesh lines perpendicular to the dimension is K.

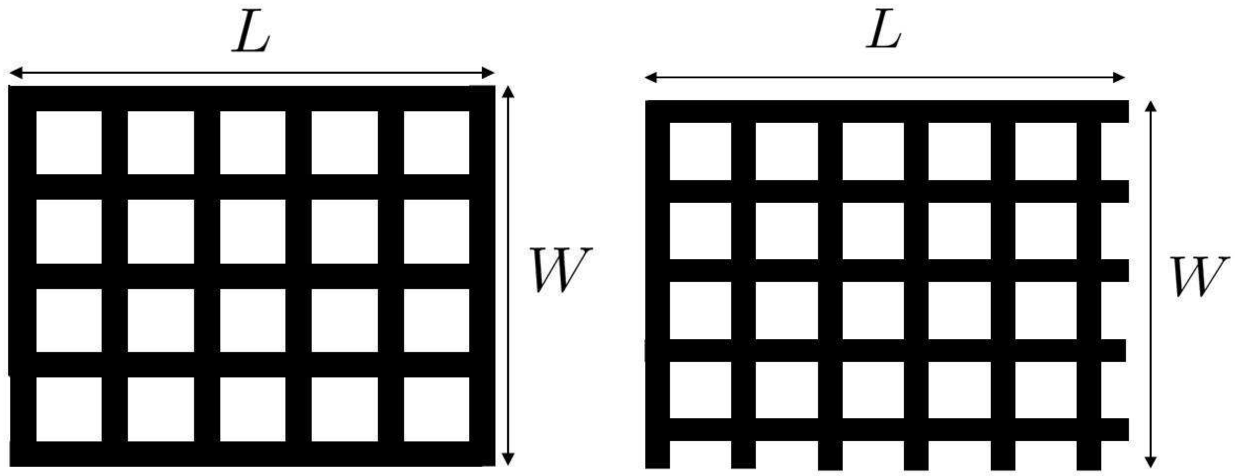

(a) Realizable dimensions

(b) Non-realizable dimensions

Figure 2.3

$$D = q + (K - 1)(p + q) \tag{2.9}$$

It is possible to design the optically transparent mesh material such that the required dimensions are realizable. In this work, a more cost effective technique is utilized from existing material since it is expensive to fabricate small batches with different pitches for the length and width dimension of an element. Additionally this material would only have use for one specific application.

The sheet resistance of the mesh material is dependent on the mesh geometries, q and p, as well as the mesh line thickness. With a mesh configuration, sheet resistances on the order of 0.052 Ω/sq are achieved [15]. The low sheet resistances allow for the conducting elements to achieve high efficiency. The sheet resistance of the mesh material is also affected by its thickness. As mentioned before with regard to skin depth, if the thickness is less than four skin depths, the sheet resistance can dramatically increase.

Table 2.1 tabulates the sheet resistance and optical transparency of the three different optically transparent and electrically conducting materials [7, 15, 32]. Having a low sheet resistance and a high optical transparency is desired, and this table shows that no one material performs best over both metrics. The mesh grid material has the lowest sheet resistance, which is most desirable for the performance of a conducting element.

Material	Sheet Resistance (Ω/sq)	Optical Transparency (%)
Conductive Polymers	100	70.7
Transparent Conducting Oxides	4.6	90
Mesh Grid	0.052	80.3

Table 2.1: Properties of transparent and electrically conducting material

2.3 Patch Antenna

A microstrip patch antenna is a low profile antenna, which can be used in various high performance applications [34]. The complete resonating element consists of a patch antenna and an impedance matching network. This section presents the design procedure for the patch element along with various feeding mechanisms. The first part of this work involved a simulation-based analysis of two feeding mechanisms under the mesh material limitations, and these two mechanisms are described in detail after a general description is given for other techniques.

2.3.1 Patch Antenna Design

A rectangular microstrip patch antenna, shown in Figure 2.4, can be accurately analyzed for electrically thin substrates with a low dielectric constant (ϵ_r), using either the transmission-line model or cavity model [34–36]. For this thesis, the transmission-line model was used. With this model, the microstrip patch antenna is represented by two slots separated by a low-impedance (Z_c) transmission line of length L, where the dimension L is the length of the antenna. This particular design method's popularity comes from its ability to provide physical insight about the antenna based on operating parameters. This method does provide accurate results, but it may be necessary to tune the design due to the presence of fringing fields at the edges of the patch. The amount of fringing is dependent on the electromagnetic properties of the substrate as well as the physical dimensions of the substrate and patch [34].

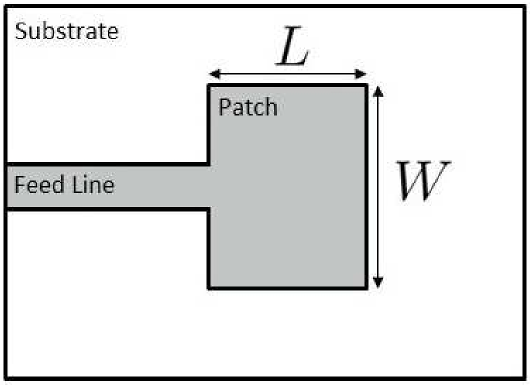

Figure 2.4: Patch antenna with edge-fed excitation

The presence of fringing fields implies waves propagate in the substrate as well as in free space above the substrate. To account for this, an effective dielectric constant ϵ_{reff} is introduced [34]. The effective dielectric constant's value is in the range of $1 < \epsilon_{\text{reff}} < \epsilon_r$ and varies with frequency (see Equation 2.11). While the fringing fields require the use of an effective dielectric constant, their presence also impacts the resonant frequency of the antenna. To achieve resonance at a desired frequency, the electrical length of the patch antenna is a half wavelength ($L_e = \lambda/2$). However, the fringing fields increase the electrical length of the patch antenna beyond the physical length. To account for this, an effective patch edge field extension (ΔL) is introduced. The dimension of the patch antenna along its length is extended on each end by this distance. The design equations for the transmission line model are presented below in Equations 2.10 - 2.13. For this method, the following operating parameters need to be specified: dielectric constant of the substrate (ϵ_r), the resonant frequency (f_r in Hz), and the substrate height (h). A description of each parameter in the equations is presented in Table 2.2.

$$W = \frac{1}{2f_r\sqrt{\mu_0\epsilon_0}}\sqrt{\frac{2}{\epsilon_r+1}} \tag{2.10}$$

$$\epsilon_{\text{reff}} = \frac{\epsilon_r+1}{2} + \frac{\epsilon_r-1}{2}\left[1+12\frac{h}{W}\right]^{-\frac{1}{2}} \tag{2.11}$$

$$\Delta L = 0.412{\cdot}h\frac{(\epsilon_{\text{reff}}+0.3)\left(\frac{W}{h}+0.264\right)}{(\epsilon_{\text{reff}}-0.258)\left(\frac{W}{h}+0.8\right)} \tag{2.12}$$

$$L = \frac{1}{2f_r\sqrt{\epsilon_{\text{reff}}}\sqrt{\mu_0\epsilon_0}} - 2\Delta L \tag{2.13}$$

$$\lambda = \frac{1}{f_r\sqrt{\epsilon_{\text{reff}}}\sqrt{\mu_0\epsilon_0}} = \frac{v_0}{f_r\sqrt{\epsilon_{\text{reff}}}} \tag{2.14}$$

2.3.2 Feeding Mechanism

There are two distinct categories used to describe various feeding mechanisms for a microstrip patch antenna: direct contact, and non-contact. The feeding techniques categorized as direct contact include edge-fed and probe-fed, while the non-contact feeding techniques include aperture coupled and proximity coupled [34, 37]. Each of these four techniques have various advantages and disadvantages associated with them. Characteristics for each feeding technique, accompanied with a general description, are presented below.

The proximity coupled feeding network consists of a grounded substrate with a microstrip

Parameter	Description
μ_0	Vacuum Permeability ($4\pi\times10^{-7}$ H/m)
ϵ_0	Vacuum Permittivity ($\sim 8.854\times10^{-12}$ F/m)
v_0	Speed of Light in a Vacuum (2.997×10^{8} m/s)
ϵ_r	Dielectric Constant
ϵ_{reff}	Effective Dielectric Constant
λ	Wavelength
f_r	Center Resonant Frequency
h	Dielectric Height
ΔL	Effective Patch Edge Field Extension
L	Patch Length
W	Patch Width

Table 2.2: Nominal antenna parameters

feed line and another dielectric substrate with a microstrip patch antenna on its top surface. A geometric layout for this feeding network can be seen in Figure 2.5a. With this feeding technique, the electromagnetic energy on the feed line is capacitively coupled to the patch antenna. The key attribute of the proximity-coupled patch is that the coupling mechanism is capacitive in nature, therefore a large impedance bandwidth is attainable [37]. However, a disadvantage of the proximity coupled feeding network is high spurious feed radiation, resulting in a reduction of the overall efficiency of the antenna [37]. Additionally, since this is a multilevel structure, alignment is crucial for optimal performance, which requires a complicated fabrication procedure.

For the aperture coupled feeding network, independent and isolated dielectric substrates are used for the feed line and patch (see Figure 2.5b for the geometry). The two substrates are isolated from each other by a common ground plane, which allows for independent

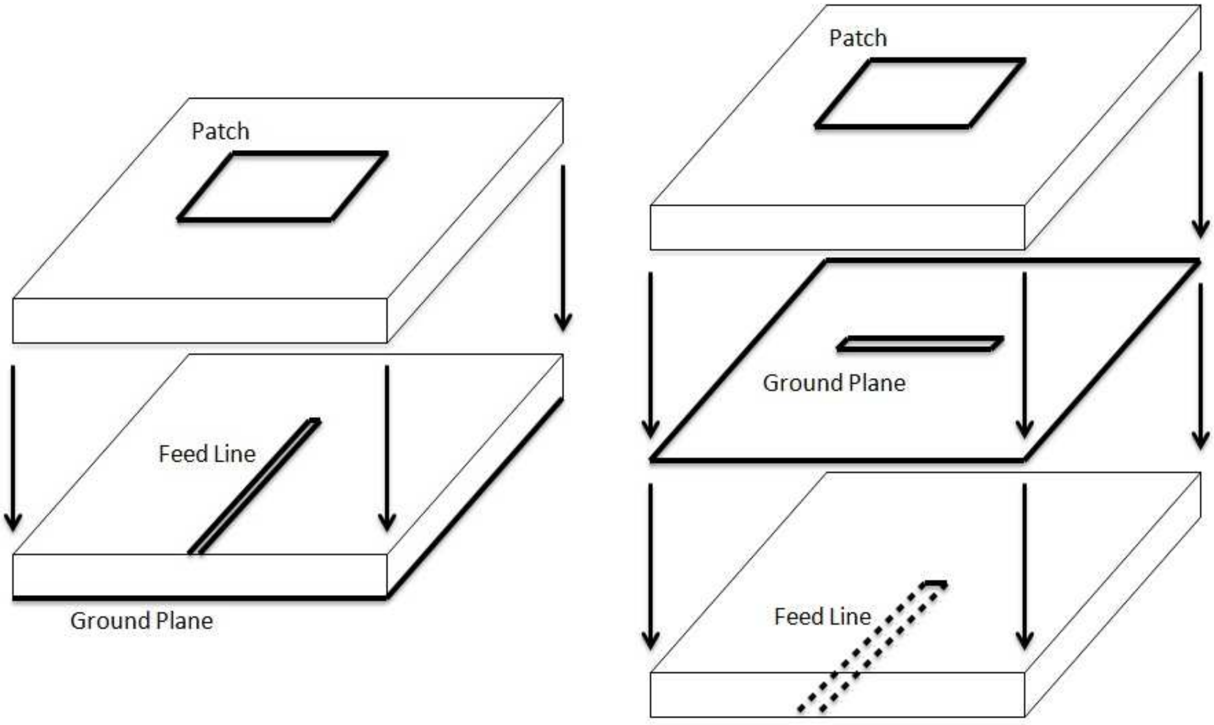

(a) Proximity coupled (b) Aperture coupled

Figure 2.5: Non-contact feeding mechanisms

optimization of the feeding mechanism and the patch element [34, 37]. With this feeding technique, the electromagnetic energy on the feed line is capacitively coupled to the antenna through the aperture in the ground plane. Just like the proximity coupled feed, the nature of the coupling mechanism is capacitive, thus allowing a large impedance bandwidth to be achieved. Another positive attribute of this mechanism is the feed line and patch element are isolated from each other, which mitigates spurious radiation [34]. However the fabrication complexity of this feeding mechanism is much higher due to an additional level of alignment being introduced. The feed line, the aperture in the ground plane, and the patch element have to be perfectly aligned for optimal performance [37].

The probe fed excitation, also referred to as the coaxial feed, utilizes a coaxial connection. The geometrical layout for this feeding technique is shown in Figure 2.6. The outer conductor is electrically connected to the ground plane, and the inner conductor extends through the substrate and is electrically connected to the radiation patch [34]. This feeding technique is efficient for thin substrates because the feeding probe is in direct contact with the antenna [36]. Additionally, most of the feed network is isolated from the patch, which reduces spurious radiation [37]. However since this is not a single layer geometry, a more complicated fabrication procedure is required. In contrast to the non-contact feeding techniques, where the geometries are simple but alignment causes complications, the probe fed excitation requires the inner and outer conductor of a single connector to be connected to different layers of the patch antenna. With this configuration, the physical length of the feeding probe imposes an upper limit on substrate thicknesses. As the length of the feed probe is increased, so is its inductance, making it very difficult to achieve quality resonance, and causing the antenna's efficiency to be compromised [37].

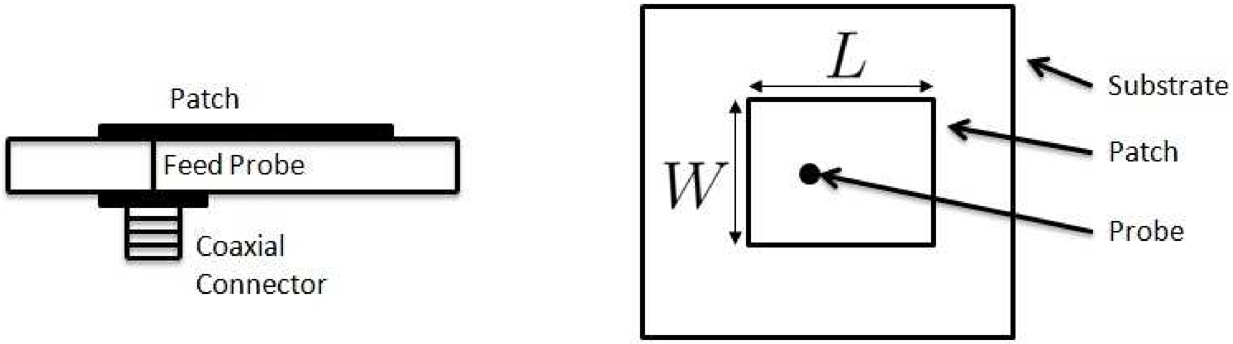

Figure 2.6: Probe-fed excitation

One of the original excitation methods for the microstrip patch antenna is the edge-fed technique [38]. The geometry for this feeding technique is shown in Figure 2.4, and it consists of a grounded substrate with a microstrip patch and feed line on the top surface. For this configuration, the feed line is directly connected to the edge of the patch antenna. Employing an edge-fed feeding technique offers many advantages. First is the ease of fabrication, since this is a single layer geometry, and both alignment and drilling requirements are removed. Second, their design and performance can be easily modeled with simple transmission line models [37], and lastly, the feeding mechanism is in direct contact with the patch antenna, resulting in a relatively high overall efficiency [34]. There are, however, disadvantages associated with this technique, such as high spurious radiation because there is no separation between the feed line and the patch antenna [34].

There are different types of edge feed configurations, for example, a quarter-wavelength impedance transformer, an inset feed, or simply a feed line with a characteristic impedance equal to the resonant impedance of the patch antenna. This work analyzed the performance of two different edge-fed techniques with optically transparent mesh material limitations, most notably, realizable dimensions. These two methods, quarter-wavelength impedance transformer and inset feed, are explained further in the following two sections.

2.3.2.1 Quarter-Wavelength Impedance Transformer

The quarter-wavelength impedance transformer is a useful impedance matching techniques that utilizes simple transmission line theory, including properties of standing waves on a mismatched line [23]. The geometry for this impedance transformer is shown in Figure 2.7.

Given a transmission line of length ℓ with a given characteristic impedance Z_0, and load impedance Z_L, the input impedance Z_{in} can be calculated as a function of its length ℓ with Equation 2.15 [20, 23], where β is the wave number ($\beta = 2\pi/\lambda$), and λ is the wavelength in the dielectric of the transmission line.

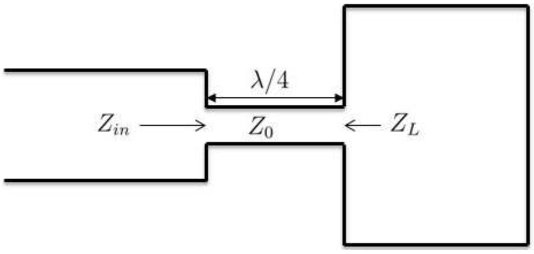

Figure 2.7: Geometry of quarter-wavelength impedance transformer

$$Z_{in}(\ell) = Z_0 \frac{Z_L + jZ_0 \tan(\beta\ell)}{Z_0 + jZ_L \tan(\beta\ell)} \tag{2.15}$$

For a transmission line with a length equal to a quarter of a wavelength ($\ell = \lambda/4$), the input impedance expression can not be evaluated directly, because the result of ∞/∞ is undefined. However, by applying L'Hôpital's rule a result can be obtained. L'Hôpital's rule states that if two functions f and g are differentiable on an open interval I containing some point c, and the following requirements are met,

- $\lim_{x\to c} f(x) = \lim_{x\to c} g(x) = 0$ or $\pm\infty$
- $\lim_{x\to c} \frac{f'(x)}{g'(x)}$ exists
- $g'(x) \neq 0$ for all x

then the following is true [39].

$$\lim_{x\to c} \frac{f(x)}{g(x)} = \lim_{x\to c} \frac{f'(x)}{g'(x)} \tag{2.16}$$

From Equation 2.15, let $f(x) = Z_L + jZ_0 \tan(\beta x)$ and $g(x) = Z_0 + jZ_L \tan(\beta x)$, where $x = \ell$ and $c = \lambda/4$, then Equations 2.15 and 2.16 can be combined to form the following,

$$Z_{in}(\ell = \lambda/4) = Z_0 \lim_{x\to\frac{\lambda}{4}} \frac{f'(x)}{g'(x)} = Z_0 \lim_{x\to\frac{\lambda}{4}} \frac{Z_0 \sec^2(\beta x)}{Z_L \sec^2(\beta x)} = \frac{{Z_0}^2}{Z_L} \tag{2.17}$$

Rearranging Equation 2.17, the characteristic impedance of the transmission line, whose length is equal to a quarter of a wavelength, can be calculated with the following expression.

$$Z_0 = \sqrt{Z_{in} Z_L} \tag{2.18}$$

This evaluation is beneficial because a quarter-wavelength impedance transformer can be used when the load impedance, Z_L, is known, and the input impedance Z_{in}, is a desired value such that a proper match can be achieved. Typically this technique is used to match a load impedance to a transmission line. Thus, the desired input impedance is equal to the characteristic impedance of the previous transmission line, and the load impedance is the input impedance of the next circuit element (the patch element). This impedance matching technique is limited to real load impedances, and provides a perfect match only at one frequency since the length is frequency dependent [23]. However, if a single quarter-wavelength impedance transformer is too band limiting, the bandwidth of the impedance matching network can be improved by employing a multisection quarter-wavelength impedance transformer with N equal length sections of transmission lines, and the impedance is gradually transformed [23].

2.3.2.2 Inset Feed

The inset feed impedance matching technique is a technique employed to reduce the resonant input impedance of the microstrip patch antenna such that it matches the characteristic impedance of the feed line [34]. Typically the resonant input impedance of a microstrip patch antenna is in the range of 150 Ω - 300 Ω [37]. The high impedance at the edge of the patch is due to the voltage and current characteristics on the patch. At the edge of the patch, the voltage is at a maximum, and the current is at a minimum [34]. However, the magnitude of the current increases, and the voltage decreases toward the center of the patch and therefore the input resonant impedance decreases. Figure 2.8 shows the geometrical representation of a patch antenna with an inset feed, where the feed is recessed a distance d into the patch.

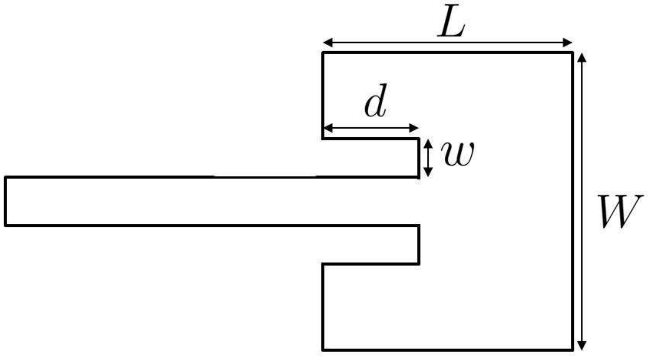

Figure 2.8: Geometry of inset feed matching technique

Through experimental results, Equation 2.19 was found, and is used to calculate the resonant input impedance of the microstrip patch antenna [34].

$$R_{in}(d) = R_{in}(0)\cos^2\left(\frac{\pi}{L}d\right) \tag{2.19}$$

A normalized plot of this equation can be seen in Figure 2.9. Both axes of this figure are normalized. On the y-axis, the resonant input impedance is normalized by the edge input impedance $R_{in}(0)$, and on the x-axis, the inset feed distance d is normalized by the length of the antenna L.

The inset feed introduces two physical notches in the antenna, which introduces parasitic capacitance [34]. The physical notch and associated parasitic capacitance slightly influences the resonant frequency, requiring the patch antenna dimensions to be tuned in order to maintain the desired resonant frequency. Additionally, maintaining a proper match requires highly accurate dimensions. Due to the nature of how the impedance varies, as observed from

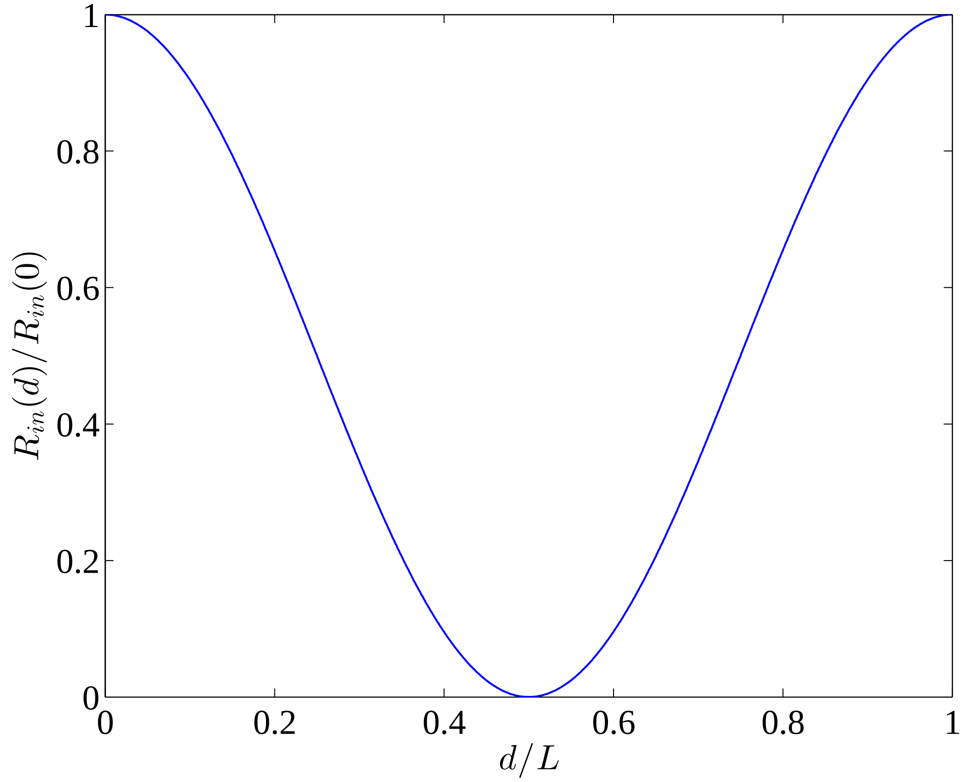

Figure 2.9: Normalized resonant input impedance

Equation 2.19 and Figure 2.9, the input impedance changes slowly as the feed point is close to the edge of the patch. However as the inset feed depth increases further into the center of the patch, the input impedance varies rapidly. In addition to dimensions being critical for a proper match, material parameters need to have a tight tolerance, since they influence the dimensions. Variations in material parameters, (relative permittivity ϵ_r, substrate thickness (h), etc.) can result in the loss of the proper match between the antenna and the feed line.

2.4 Antenna Array

In general, a single antenna element has a wide radiation pattern and a low gain (directivity) [34]. There are however, various applications, such as long distance communication, where it is desired to have a very directive antenna, and consequently, higher gain. For such applications, directional antennas and antenna arrays can be used as they can provide high directivity. An antenna array is an assembly of single radiating elements deployed in a particular geometrical configuration. There are several configurations which can be used, for example, linear, circular, rectangular, or spherical. The initial design of this work utilized a uniform linear array (ULA), and as such the remainder of this section describes the characteristics of a ULA.

2.4.1 Uniform Linear Array (ULA)

A uniform linear array or phased array is an array of identical elements, which are fed with variable phase or time-delay controls at each element to direct the overall antenna's beam to given angles in space [40]. The energy is directed through constructive and destructive interference of each element, which is referred to as beam steering [34]. Beamsteering is achieved easily with a uniform linear array because the signal sent to each element has the same amplitude, and a progressive phase shift $\Delta\phi$ whose value is determined depending on the desired steering direction [34]. For an N element array, the phase delay of the n^{th} element is calculated with Equation 2.20 [41], where λ is the wavelength, d is the separation distance between the elements in the array, and θ is the angle associated with the desired radiation direction (relative to the vertical axis), see Figure 2.10.

$$\phi_n = \frac{2\pi}{\lambda}(n-1)d\sin\theta \tag{2.20}$$

The primary reason for using a phased array, where the phase delays are electronically controlled, is the speed at which the steering direction can be changed [40]. With traditional fixed directional antennas, the physical apparatus has to be repositioned in order to change

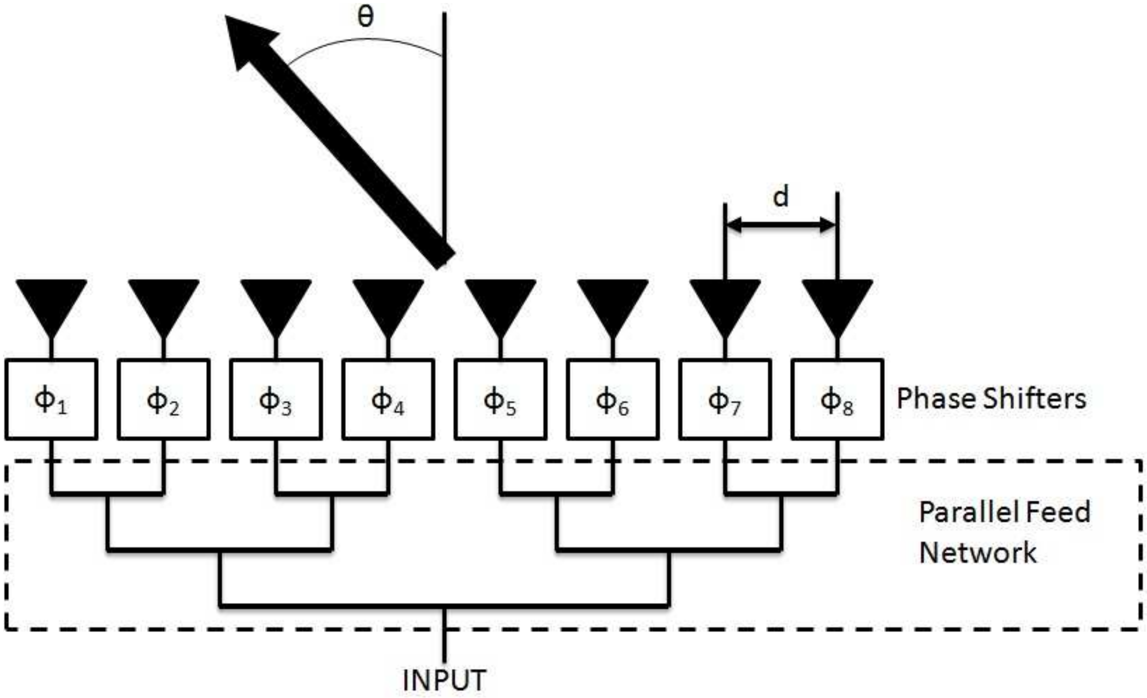

Figure 2.10: N element antenna array ($N = 8$)

the radiation direction.

It was not until the late 1980s that patch antennas were used in phased arrays for beam-steering applications [42]. Their use was eagerly adopted, since it can be relatively simple to fabricate an array of patch elements due to the nature of a patch element essentially being a two dimensional antenna, and printing multiple patches and feed lines on a single layer was just an extension of already existing printing technology [36]. Additionally, this technology can be used regardless of the feeding mechanism (direct contact edge-fed or non-contact coupled-fed), since each layer does not require complex three dimensional printing [36].

2.5 Simulation and Experimental Test Setup

In this section, ANSYS® High Frequency Structure Simulator (HFSS) and the anechoic chamber are discussed. HFSS is a computational electromagnetic solver used to model the antenna's performance for simulation-based analyses, while the anechoic chamber was used to empirically measure the antenna's performance.

2.5.1 Computational Electromagnetic Solver

ANSYS® High Frequency Structure Simulator (HFSS) is a simulation software package used for electromagnetic modeling of complex 3-D geometries. Through the multiple state-of the-art solver technologies based on finite element, integral equation, or advanced hybrid methods offered by HFSS, a wide range of microwave, RF, and high-speed digital applications can be solved with high accuracy [43]. For this work, HFSS was used to model the performance of the antenna with performance metrics such as scattering parameters and radiation patterns. Figure 2.11 shows an antenna as an HFSS object with its radiation pattern.

2.5.2 Anechoic Chamber

An anechoic chamber is a room designed to produce a testing environment for RF systems. The inside walls of the chamber absorb all reflected electromagnetic energy, while the outer walls form a Faraday Cage, shielding the inside of the chamber from external electromagnetic energy. Typically, an anechoic chamber is used for performance measurements of antenna radiation patterns, as well as electromagnetic interference (EMI) and electromagnetic compatibility (EMC) testing. For this work, the antenna's gain and radiation patterns were measured in an anechoic chamber. The inside of the anechoic chamber shown in Fig-

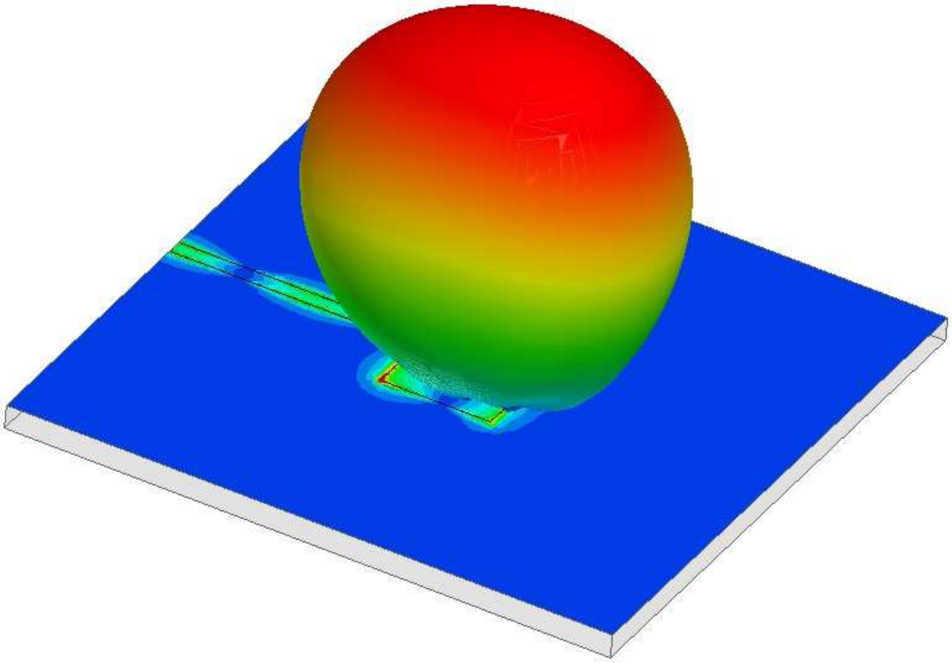

Figure 2.11: 3-D radiation pattern in HFSS

ure 2.12 has a positioner, on the left, and a horn antenna, on the right. The positioner was used to mount the antenna under test (AUT) while the horn antenna was used to transmit the source signal for the AUT to receive. Based on the power received by the AUT, the gain was calculated. The calibration procedure as well as a close-up image of the positioner and horn antenna for the anechoic chamber used, can be seen in Appendix B.

Figure 2.12: Inside the anechoic chamber

CHAPTER 3

Optically Transparent Patch Antenna Design

3.1 Introduction

Several challenges exist with the design of a microstrip patch antenna and its feeding mechanism composed of optically transparent mesh material. The performance of edge-fed feeding mechanisms depends on transmission line properties such as width and RF impedance. Previous work utilized a probe-fed excitation, removing the optically transparent mesh material from the feeding network. One contribution of the work presented in this chapter is an analysis of these transmission line properties utilizing a mesh transmission line. To investigate these transmission line properties of the mesh material, a simulation-based analysis of two edge-fed feeding mechanisms was performed. The two feeding mechanisms selected for analysis were the inset feed and the quarter-wavelength impedance transformer. Performance metrics such as scattering parameters and individual antenna radiation patterns were analyzed for both feeding mechanisms. Using these metrics, the inset feed was shown to outperform the quarter-wave impedance transformer. This analysis was performed using ANSYS® High Frequency Structure Simulator (HFSS) software package.

3.2 Optically Transparent Mesh Material Geometry

The geometry of the optically transparent copper mesh material used for the antennas, has a line width, q, of 23.9 μm and a pitch, p, of 301.3 μm, and the copper mesh lines have a thickness of 4.3 μm. This geometry was chosen based on previously considered geometries [15] as well as commercially available products, as it is more cost effective to utilize already existent material than to require specific fabrication. With the parameters of this mesh material, a sheet resistance of 0.68 Ω/sq and optical transparency of 85.8% were achieved. Additionally, the skin depth of copper at 5.5 GHz is ~0.898 μm. Thus, the copper thickness is greater than four skin depths and will not introduce any additional resistance. These dimensions are used when creating the optically transparent antenna objects for simulations in HFSS, as well as calculating the realizable dimensions for the antennas, which was done using Equation 2.9. The optical transparency of this material is qualitatively shown in Figure 3.1, where the optically transparent mesh material is overlaid on an image of the University of New Hampshire's logo. Additionally, a mocked-up grid structure is included to illustrate the material's line width q and pitch size p.

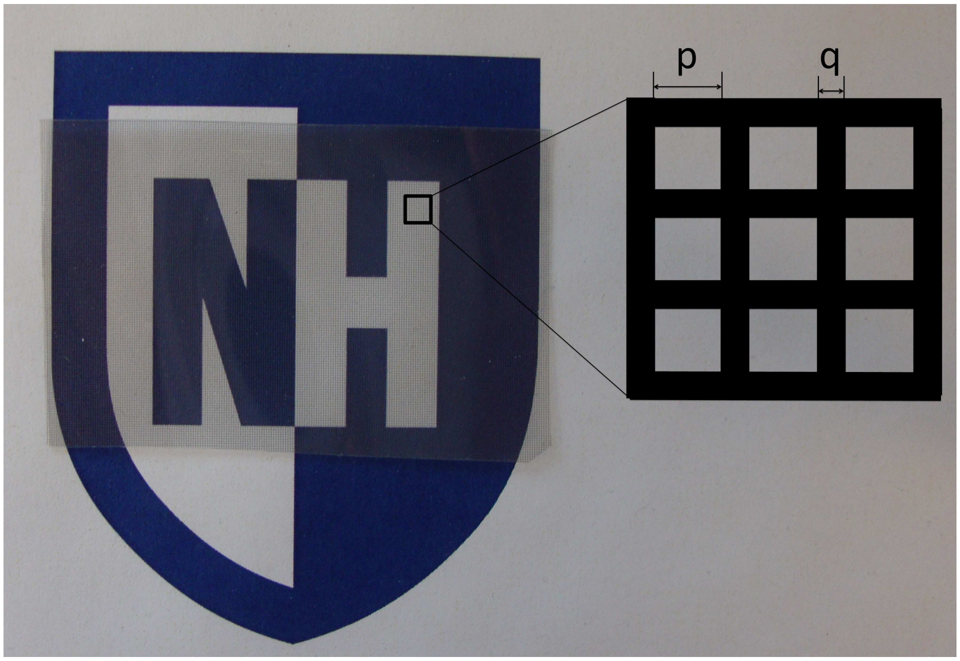

Figure 3.1: Optically transparent copper mesh material ($p = 301.3$ μm and $q = 23.9$ μm)

3.3 Microstrip Patch Antenna Design

The microstrip patch antenna was designed with the equations presented in Section 2.3.1. Using the operating parameter values presented in Table 3.1, the length and width of the antenna were calculated to be 14.5 mm and 19.9 mm respectively. Using these dimensions, antennas were simulated in HFSS.

ϵ_r	2.75
f_r	5.5 GHz
h	3.175 mm (1/8 inch)

Table 3.1: Patch antenna operating parameter values

The design procedure outlined in Section 2.3.1 provides accurate results. However, the presence of fringing fields around the edges of the patch antenna require dimensions to be tuned to resonate as desired. Therefore, a solid copper antenna was simulated and tuned to resonate properly at 5.5 GHz. The length and width of the properly tuned patch antenna were determined to be 14 mm and 19.9 mm respectively. Using these dimensions along with Equation 2.9, the dimensions for the optically transparent patch antenna were determined. Table 3.2 shows the calculated realizable dimensions closest to the desired dimensions for the optically transparent mesh antenna and the number of mesh lines (K) perpendicular to the dimension.

Dimension	Desired Value	Realizable Value	Difference (%)	K
Length	14 mm	14.0075 mm	0.05 %	44
Width	19.9 mm	19.8611 mm	0.19 %	62

Table 3.2: Optically transparent mesh patch antenna dimensions

With the physical dimensions of the patch element calculated, the next section to design was the feeding network.

3.4 Feeding Network

Feeding the antenna with a transmission line that has a characteristic impedance equal to the input impedance of the antenna is not practical as it would require a transmission line with unfeasible width. Additionally, using the optically transparent material limits the realizable widths. Figure 3.2 shows the RF impedance of the feed line is asymptotically related to the number of mesh lines. The RF impedance was calculated using transmission line theory equation presented in Appendix C. As a result of this, the sensitivity of the feed line's impedance increases as the number of mesh lines decreases. Therefore, it is desired to have a lower characteristic impedance as small changes in the number of mesh lines will not drastically change the feed line characteristic impedance. This finding is one of the contributions presented in this chapter. The initial designs were done using a 50 Ω feed line. This impedance was chosen because all of the measurement equipment used has a 50 Ω output port, as well as the relationship between the RF impedance and number of mesh lines.

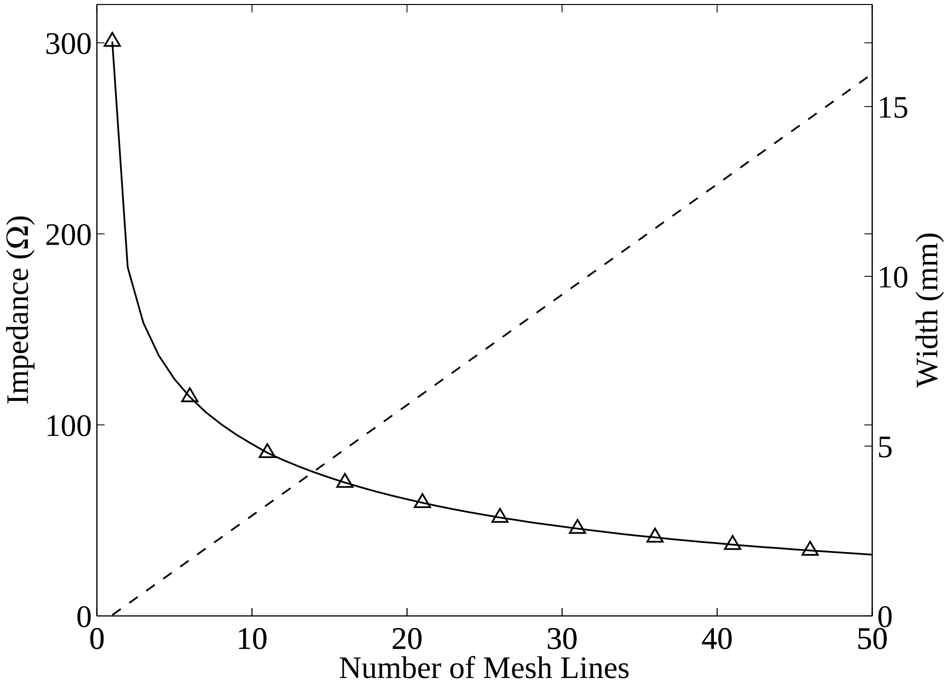

Figure 3.2: Characteristic impedance (△) and width (--) of feed line as a function of the number of mesh lines

In this section, two edge-fed designs are presented, and in a future section their performance is analyzed and compared under the mesh material limitations. While the first feeding network design employs a quarter-wavelength impedance transformer to match the antenna's impedance to the characteristic impedance of the feed line, the second utilizes the inset feed technique to reduce the resonant input impedance of the patch antenna to match the characteristic impedance of the feed line. Through HFSS simulations, the resonant input impedance for the solid copper antenna and the optically transparent antenna resonators were determined to be 300 Ω and 285 Ω respectively.

3.4.1 Quarter-Wavelength Impedance Transformer

The quarter-wavelength impedance transformer feeding network was composed of two sections. For each section, the transmission line had a unique characteristic impedance. While the first section was a microstrip transmission line with a characteristic impedance (Z_1) of 50 Ω, the second section was the quarter-wavelength impedance transformer. The impedance transformer was used to match the 50 Ω transmission line to the patch antenna, and had a characteristic impedance Z_2. The design procedure was followed as outlined in Section 2.3.2.1. For this design, the desired input impedance (Z_{in}) was 50 Ω, and the load impedance (Z_L) was 300 Ω and 285 Ω respectively for the solid copper and optically transparent resonators. Using Equation 2.18 the characteristic impedances for the quarter-wavelength impedance transformers were calculated to be 122.5 Ω and 119.4 Ω respectively. Each microstrip transmission line was designed based on the physical and electromagnetic properties of the Lexan substrate as well as the desired characteristic impedance. Using transmission line theory equations presented in Appendix C, the widths of the 50 Ω, 122.5 Ω, and 119.4 Ω transmission lines were calculated to be 8.5 mm, 1.6 mm, and 1.54 mm respectively. Additionally, the length of both quarter-wave impedance transformers was calculated to be 9.2 mm. Table 3.3 shows the calculated realizable dimensions for the 50 Ω transmission line and the quarter-wavelength impedance transformer feeding network made of the optically transparent mesh material, as well as the number of mesh lines (K) perpendicular to the dimension.

Dimension	Desired Value	Realizable Value	Difference (%)	K
Length ($\lambda/4$)	9.2 mm	9.1295 mm	0.76 %	29
Width ($\lambda/4$)	1.54 mm	1.6499 mm	7.2 %	6
Width (50 Ω)	8.5 mm	8.4791 mm	0.24 %	27

Table 3.3: Quarter-wavelength impedance transformer feeding network dimensions composed from optically transparent mesh material

3.4.2 Inset Feed

Using a 50 Ω feed line, the depths of the inset feed necessary to match the resonant input impedance of the patch antenna were calculated, using Equation 2.19, to be 5.13 mm and 5.08 mm for the solid copper and optically transparent resonators, respectively. As stated before, due to the transmission line width sensitivity, it is desired to have a low characteristic impedance (or wider transmission lines). However, lower impedances will result in inset feeds that reduce the antenna's effective length, due to the depth of the inset matching slots, resulting in the resonant frequency increasing [34]. This effect can be mitigated by increasing the physical length of the antenna until the resonant frequency has shifted back to what is desired, or by reducing the depth of the inset feed. To reduce the depth of the inset feed, the characteristic impedance of the feed line must be increased, which in turn decreases the feed line's width.

The use of an inset feed requires a balance between these two effects. Therefore, the characteristic impedance of the feed line was increased from 50 Ω to 100 Ω, and the length of the patch antenna was increased to 14.6 mm from 14.0 mm. The transmission line theory equations presented in Appendix C were used to calculate the width of the 100 Ω transmission line to be 2.2 mm.

With the new antenna length and transmission line characteristic impedance, the inset feed depth was calculated using Equation 2.19 to be 3.75 mm and 3.6 mm for the solid copper and optically transparent resonators, respectively. In addition to the depth, the inset feed has a slot width associated with it. The value of this was determined for the solid copper antenna through an iterative simulation to be 1.25 mm. Due to the difficulty in iterating through inset feed slot widths for the optically transparent resonator, the slot width was determined based on the closest realizable dimension to the width of the solid copper antenna. Table 3.4 shows the calculated realizable dimensions for the new antenna length (L), as well as the inset feed depth (d) and width (w), along with the number of mesh lines (K) perpendicular to the dimension.

Dimension	Desired Value	Realizable Value	Difference (%)	K
Depth (d)	3.6 mm	3.6011 mm	0.03 %	12
Width (w)	1.25 mm	1.3247 mm	5.9 %	5
Length (L Antenna)	14.6 mm	14.6579 mm	0.39 %	46
Width (Feed line)	2.2 mm	2.3003 mm	4.56 %	8

Table 3.4: Inset feed feeding network dimensions composed from optically transparent mesh material

3.5 Simulation Performance

With the design of these two sets of antennas complete, the object geometry was constructed and simulated in HFSS. Prior work has shown that the mesh material behaves similar to a solid piece of copper, and therefore all simulations used a solid conducting ground plane to approximate the mesh material. While this approximation reduced computations, the resonating element was made from the mesh material to get a more accurate understanding of how it behaved. The performance of the antennas with the different feeding mechanisms were analyzed using the system's scattering parameters as well as the antenna's radiation pattern. Scattering parameters are used to determine the band of frequencies over which the antenna is approximately resonant, while the radiation pattern in used to show where the antenna is radiating spatially. For each performance metric, both feeding mechanisms are analyzed for both antennas.

3.5.1 Scattering Parameters

These antennas are a one-port network, and as such the only scattering parameter to observe is the S_{11} of the system, which is the reflection coefficient. This is a measure of how much energy is reflected back to the generator. A high reflection coefficient means less energy can be transmitted. Figure 3.3 shows the reflection coefficient expressed in dB for the solid copper and the optically transparent mesh antennas over a solid copper ground plane. More specifically, Figure 3.3a shows the scattering parameters for both feeding techniques for the solid copper antenna, and Figure 3.3b shows the scattering parameters for both feeding techniques for the optically transparent antenna.

Both feeding mechanisms for the solid copper antenna perform similarly. Using the

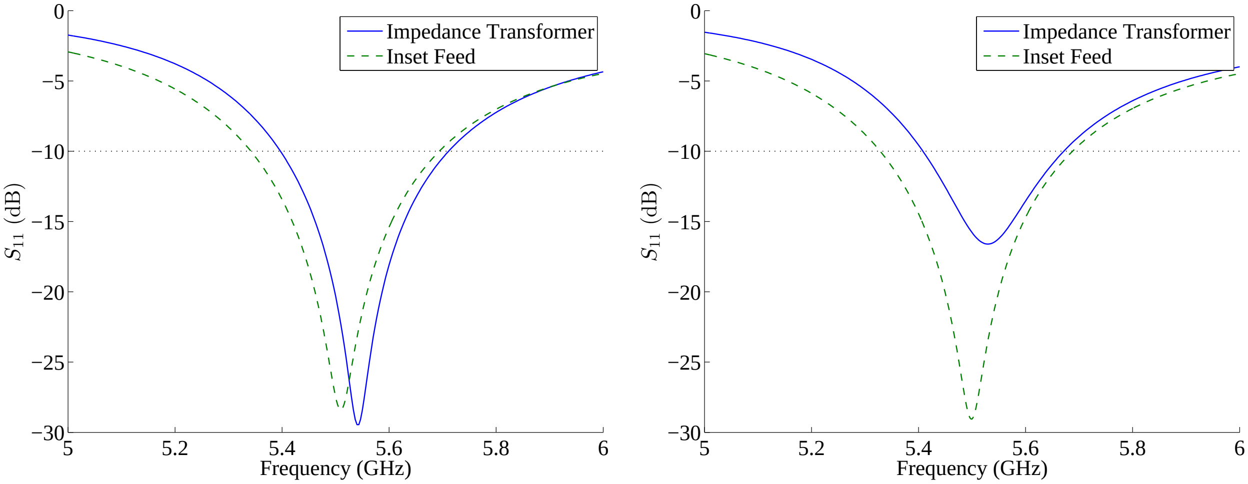

(a) Solid copper antenna (b) Optically transparent mesh antenna

Figure 3.3: Magnitude of the reflection coefficient (S_{11}) in dB

quarter-wave impedance transformer, a 10 dB return loss bandwidth of 5.6% centered at 5.54 GHz was achieved, and a bandwidth of 6.4% centered at 5.51 GHz was achieved using the inset feed. Additionally, the maximum return loss is very high and there is approximately one dB difference between them. For the optically transparent antenna however, both feeding mechanisms do not have a similar performance. The bandwidth achieved using the inset feed is 6.5% centered at 5.5 GHz, while the bandwidth achieved using the quarter-wave impedance transformer is merely 4.7% centered at 5.53 GHz. Furthermore, there is a 12.44 dB difference between the maximum return loss from both feeding mechanisms. Using the inset feed, a maximum return loss of 29.05 dB is achieved while the maximum return loss achieved when using the quarter-wave impedance transformer is 16.61 dB. The poor performance of the quarter-wave impedance transformer is a result of the realizable dimensions limiting the widths of the transmission lines necessary to achieve a proper match. Table 3.3 shows the percent difference between the desired value and the actual value is highest for the width of the quarter-wave impedance transformer. It may be possible to achieve realizable dimensions and a better match using a multisection impedance transformer, as described in Section 2.3.2.1. However, with manufacturability in mind, this would be a more complicated design to fabricate.

Figure 3.4 compares the reflection coefficient for the solid copper and optically transparent antennas with the inset feed matching mechanism. Graphically, it is clear that both antennas have a very similar performance. Table 3.5 shows the performance of the inset feed for the solid copper and optically transparent antennas based on the simulated scattering parameters.

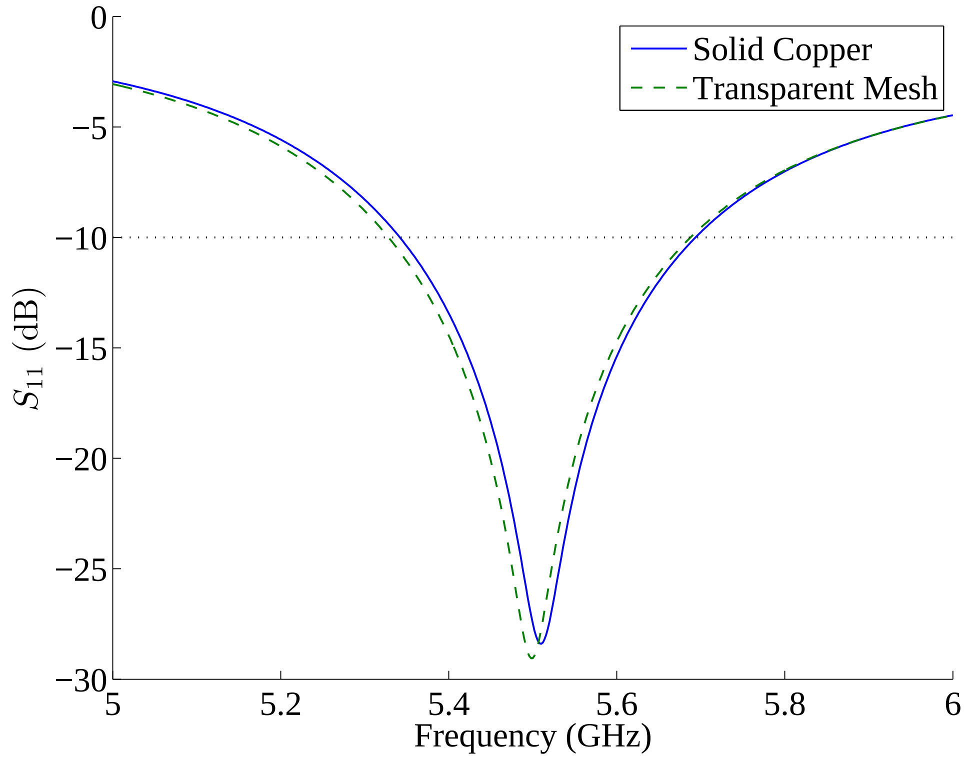

Figure 3.4: Reflection coefficient for inset feed excitation

Antenna	Center Frequency f_c (GHz)	Bandwidth (% of f_c)	Return Loss Maximum (dB)
Solid Copper	5.51	6.4	28.4
Transparent Mesh	5.5	6.5	29.05

Table 3.5: Antenna performance with inset feed based on scattering parameters

3.5.2 Radiation Pattern

In addition to the scattering parameters, the performance of the two feeding mechanisms was analyzed using the antennas' radiation patterns. In Figure 3.5 azimuthal plane radiation patterns are presented for both antennas with each feeding mechanism. The desired center resonant frequency was 5.5 GHz, and as such the radiation patterns presented here are for the antenna operating at 5.5 GHz. In HFSS, the antenna's absolute gain values in dBi were not determined, and therefore each radiation pattern is individually normalized. As a result of this, the performance metric associated with these radiation patterns is the antenna's beamwidth, which is calculated using the -3 dB point.

The performance of both antennas for each feeding technique based on the radiation pattern is nearly the same. The solid copper antenna feed with either mechanism achieved a 70° beamwidth while the optically transparent mesh antenna achieved a 72° beamwidth. Additionally, all antennas have a front to back ratio which is greater than 20 dB, meaning nearly all of the power is radiated above the patch, as desired. The simulated performance of these antennas also illuminates the possibility of approximating a mesh grid structure with solid copper object. This is advantageous as the simulations with the mesh geometry are computationally taxing and an iterative process to tune a design is not practical.

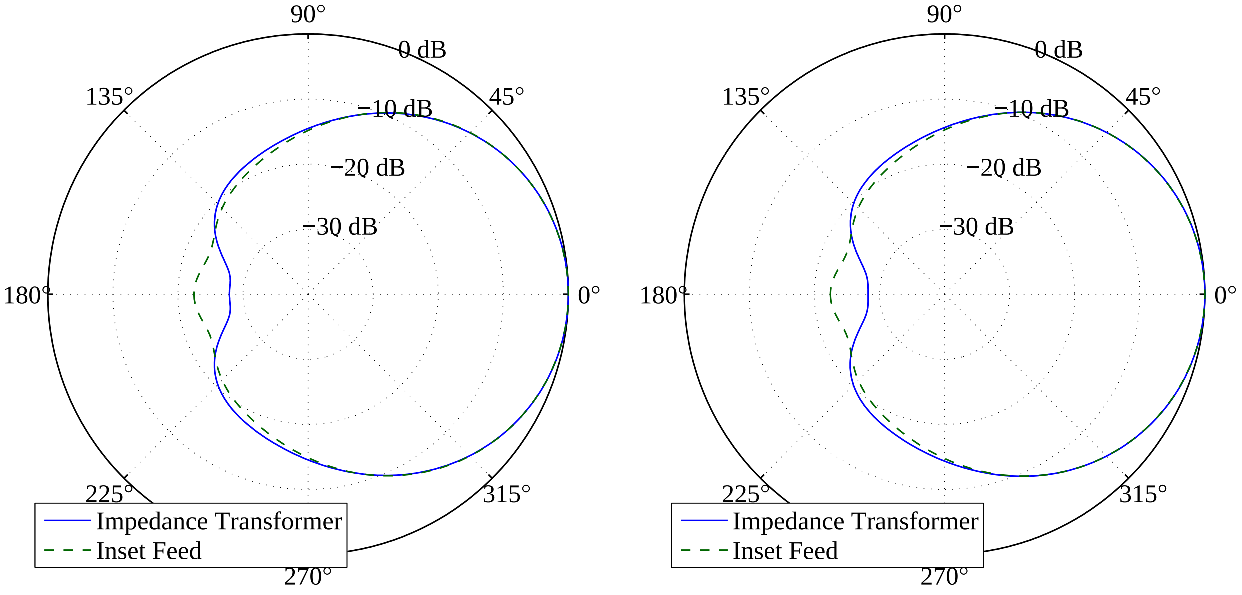

(a) Solid copper antenna (b) Optically transparent mesh antenna

Figure 3.5: Azimuthal plane radiation pattern

In this chapter, it was shown that when feeding an antenna it is desired to have the characteristic impedance of the transmission line low to reduce the sensitivity to small variations in the trace width. This is more prominent with the optically transparent mesh material because there are discrete realizable dimensions. This introduces challenges associated with the feeding mechanism of an optically transparent microstrip patch antenna. In the analysis above, the performance of the quarter-wavelength impedance transformer and inset feed feeding techniques were compared under the limitations of the optically transparent mesh material using the scattering parameters and aspects of the radiation patterns as performance metrics. Since the radiation patterns were normalized, the only aspect used was the beamwidth, and this did not show any indication as to which feeding technique had a better performance. However, when analyzing the performance of the two feeding techniques with the scattering parameters, it is clear the inset feed outperforms the quarter-wave impedance transformer. Using the inset feed, the optically transparent antenna achieved a larger bandwidth and a larger return loss, which shows the antenna functions over a larger frequency range and has less energy reflected back to the transmitter. This proves the inset feed is superior to the quarter-wavelength impedance transformer under the limitations of the optically transparent mesh material. In the next chapter, the procedure taken to fabricate a solid copper and optically transparent antenna with an inset feed is presented.

CHAPTER 4

Fabrication Procedure

4.1 Introduction

After successfully simulating an optically transparent antenna composed of a highly conductive copper mesh over a solid copper ground plane, the designed antenna was physically constructed with easily accessible low cost material to empirically measure the antenna's performance. Additionally, the solid copper antenna was constructed for reference purposes. The copper material used was a copper foil with a thickness of one one-thousandth of an inch. This copper material does have a greater thickness than what was simulated, in the simulation the copper thickness was set to 4.3 μm based on the thickness of the copper in the mesh material. However, since both thicknesses are greater than four skin depths it was not expected to severely alter the results.

To understand the impact and functionality of using optically transparent mesh material for the antenna, four antennas were constructed and measured. The first antenna had a solid copper resonator, while the second utilized the optically transparent mesh material for the resonator. Each of these antennas had a solid copper ground plane. This configuration allowed for an analysis of the optically transparent material when used as a resonator, with the ground plane kept as a control. After the performance of the two antennas was measured, the solid copper ground planes were removed and replaced with the optically transparent mesh material, and the antennas' performance was measured. This configuration allowed for an analysis of the two antennas with the resonator kept as a control. The advantage of this measurement campaign was to isolate the performance of the mesh material as the ground plane. The following sections in this chapter outline the procedure taken to fabricate these antennas.

4.2 Cutting The Resonator

In radio frequency engineering, accurate dimensions are critical for the product to yield proper functionality. In the 5 to 6 GHz frequency band, submillimeter variations in the patch antenna's length can cause the center frequency to shift by up to 600 MHz, resulting in an antenna resonating in the wrong spectrum, Figure 4.1 shows the resonant frequency of a patch antenna as a function of sub-millimeter variations in the patch length. Therefore,

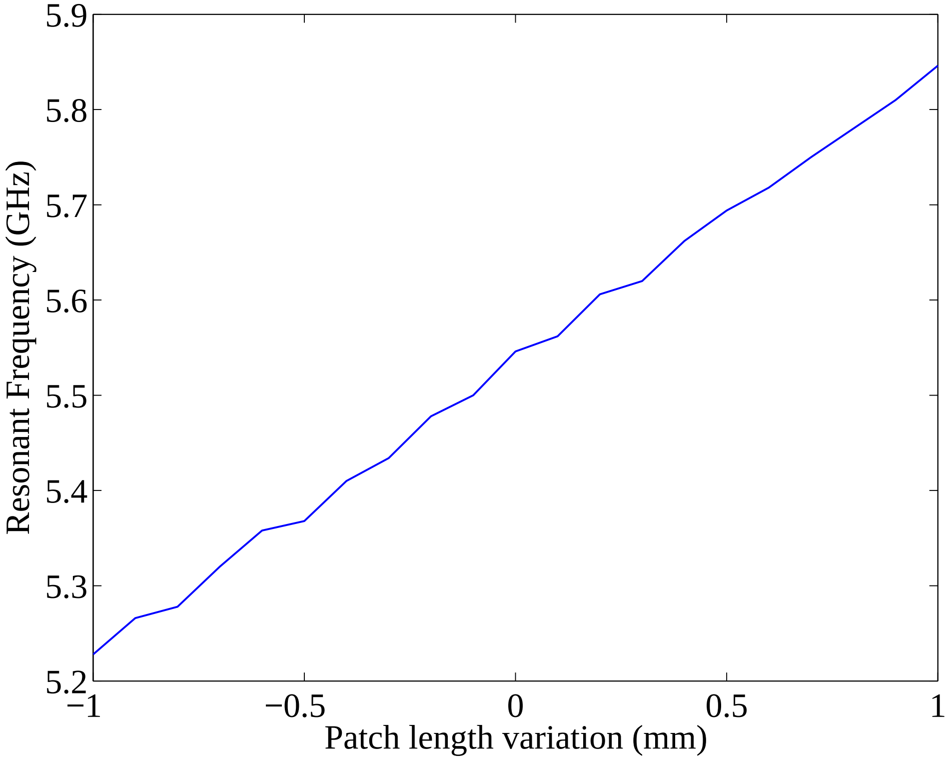

Figure 4.1: Resonant frequency shift for patch length variations

to ensure highly accurate dimensions, a jig was made for both resonators. Figure 4.2 shows the jig for the solid copper antenna resonator. The jigs were machined using a three axis ProtoTRAK milling machine.

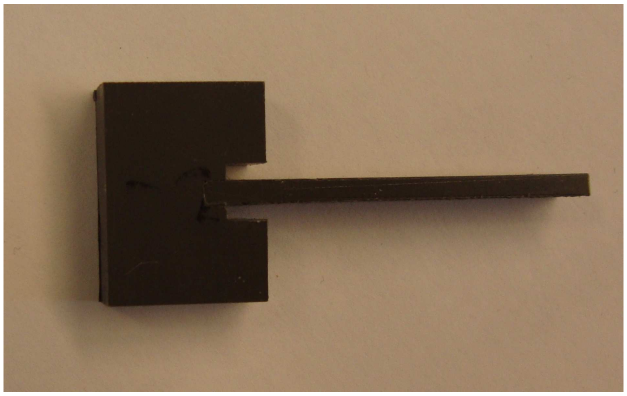

Figure 4.2: Patch antenna resonator jig

The resonators of the fabricated antennas were cut by hand with an X-Acto knife, using the jigs. Figure 4.3 shows the two hand-cut resonators.

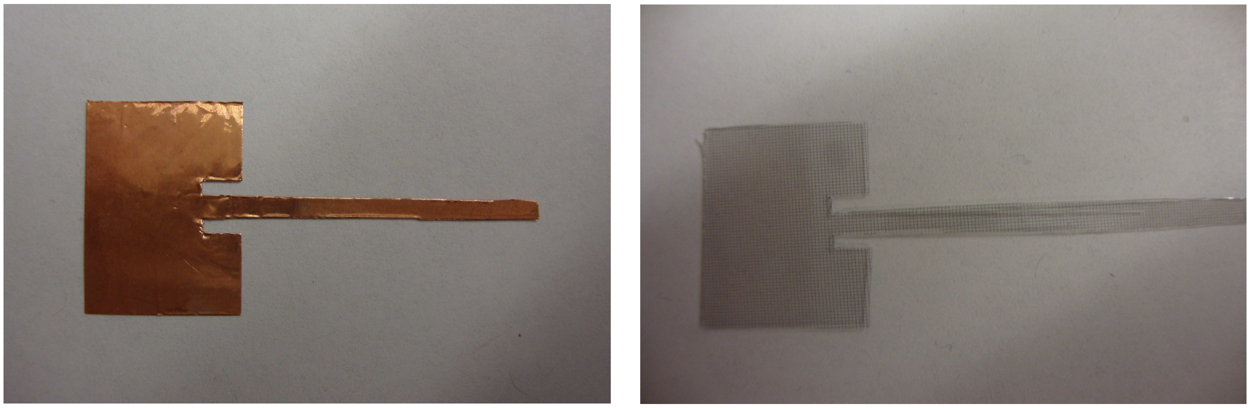

(a) Solid copper resonator

(b) Optically transparent resonator

Figure 4.3: Hand-cut resonators

4.3 Cutting the ground plane and substrate

After cutting the two resonators from their respective materials, two pieces of Lexan were cut to the appropriate size to be used as the substrate. Dimensions for the substrate were not of critical importance and were cut with a bandsaw, and the rough edges were smoothed using a grinding wheel. The ground planes were cut from the copper foil and optically transparent mesh material, using the substrate size as a stencil. Figure 4.4 shows the properly cut Lexan substrate as well as the copper foil.

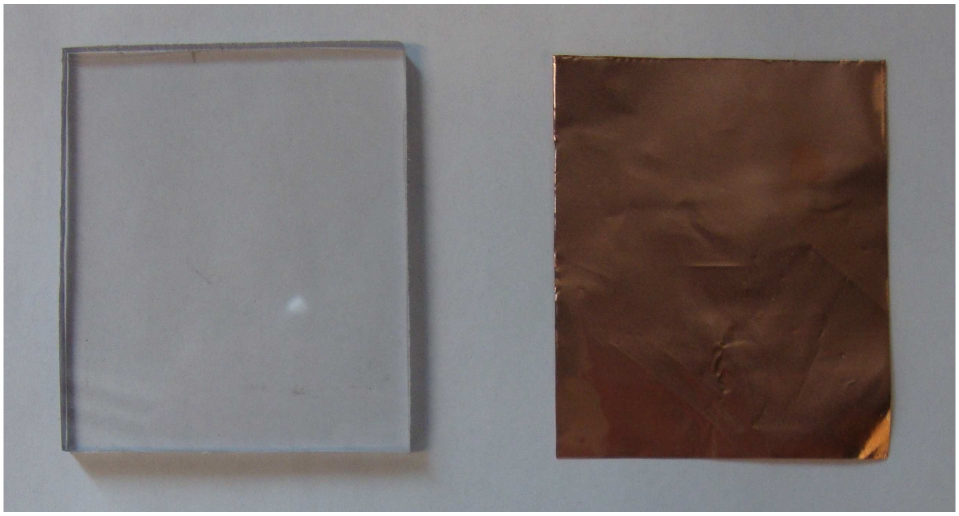

Figure 4.4: Solid copper ground plane and Lexan substrate

Using an adhesive, the resonators were adhered to their respective substrates, along with the copper foil ground plane. These antennas however, required an additional impedance matching network. As a result of the challenges associated with the design of the impedance matching network, the characteristic impedance of the transmission line feeding the antenna was increased from 50 to 100 Ω. This was easily accounted for in the simulation because the impedance of the source could be changed to 100 Ω, thus maintaining a proper match.

However, the equipment used to measure the antenna's resonance and radiation performance has a 50 Ω output port. This required an additional impedance matching network to match the 50 Ω equipment to the 100 Ω feed line to the antenna.

4.4 Design of Matching Network

The impedance matching network was responsible for matching a 50 Ω transmission line to a 100 Ω transmission line. This was done using a quarter-wavelength impedance transformer, as described in Section 2.3.2.1. For this design, the desired input impedance (Z_{in}) was 50 Ω and the load impedance (Z_L) was 100 Ω. Using Equation 2.18, the characteristic impedance of the impedance transformer was calculated to be 70.71 Ω.

This network was designed to be fabricated on FR-4 material with an operating frequency of 5.5 GHz. It is advantageous to use FR-4 material instead of Lexan, because the SMA connector could be soldered to the copper transmission line on FR-4. Soldering provides a strong electrical connection between the transmission line and the SMA connector which is connected to the measurement equipment. Due to Lexan's melting temperature of 155 °C, the SMA connector could not be soldered to the copper foil on the Lexan, because the soldering iron reaches temperatures above 300 °C and causes the Lexan to melt. If the impedance matching network were to be fabricated on Lexan, silver paste would be required. Silver paste is inferior to solder with regard to an electrical connection as well as its structural integrity. Another advantage of fabricating the impedance matching network on FR-4 is that a PCB milling machine can be used to mill the network, which is more accurate than cutting by hand with an X-Acto knife. Lastly, since the impedance matching network was fabricated using solid copper, any arbitrary dimensions necessary for the transmission lines are realizable.

The FR-4 material used has a substrate height (h) of 1.4968 mm (0.059 inches) and a relative permittivity (ϵ_r) of 4.4. Using these operating parameters, and the equations presented in Appendix C, the widths of the 50 Ω and 70.71 Ω transmission lines were calculated to be 2.86 mm and 1.5 mm respectively. Additionally, with an operating frequency of 5.5 GHz, the length of the 70.71 Ω transmission line was calculated to be 7.65 mm. The length of the 50 Ω transmission line is not of concern as it matches the impedance of the equipment. A preliminary assessment of the functionality of the quarter-wavelength impedance transformer was performed in HFSS.

4.4.1 HFSS Simulation

In HFSS, the quarter-wavelength impedance transformer was modeled as a two port network, with port one assigned as the source and port two assigned as the antenna. The impedances of port one and port two were assigned 50 and 100 Ω respectively. Figure 4.5 shows the quarter-wavelength impedance transformer object in HFSS. For proper functionality, it is desired to have a high return loss and a low insertion loss over the 5 to 6 GHz

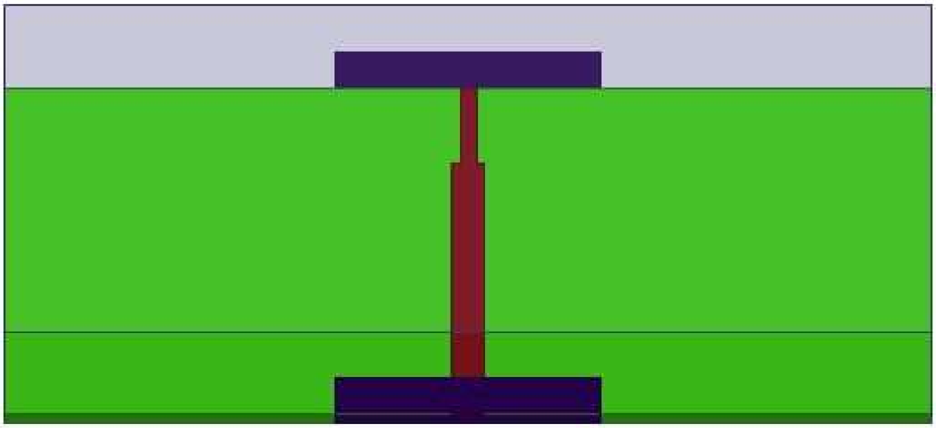

Figure 4.5: Quarter-wavelength impedance transformer object in HFSS

frequency band. If the single section impedance transformer is too band-limited, then a multisection impedance transformer can be used, as described in Section 2.3.2.1.

Figure 4.6 presents the simulation results for the scattering parameters expressed in dB. The return loss and insertion loss are easily calculated from the scattering parameters when expressed in dB. The return loss is the negative of the reflection coefficient (S_{11}) in dB, and the insertion loss is the negative of the forward gain (S_{21}) in dB. These results show S_{11} is below -25 dB, and the S_{21} is greater than -0.7 dB over the entire 5 to 6 GHz frequency band. This indicates that the impedance transformer functions as desired.

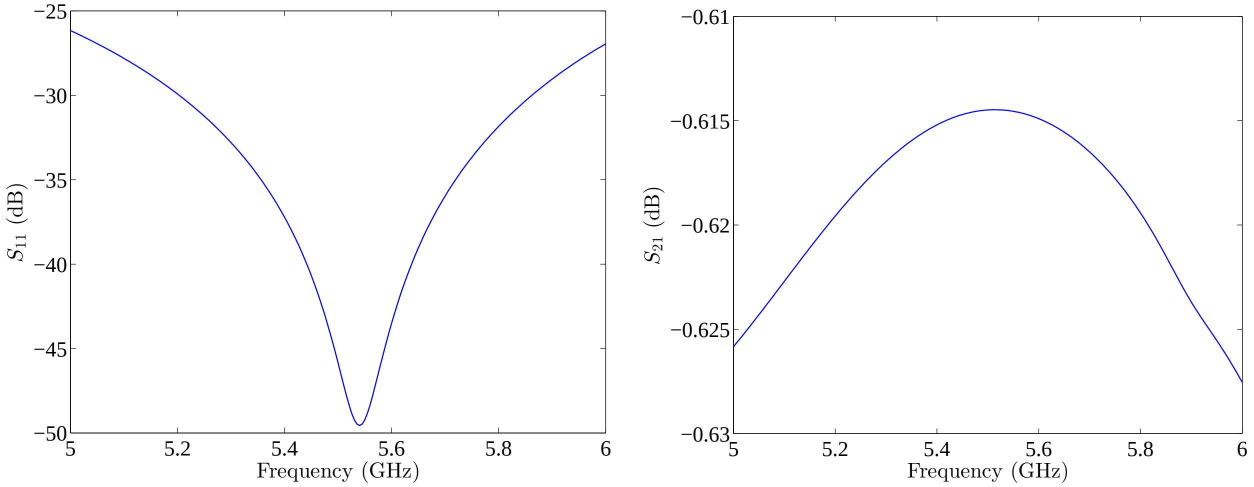

(a) Reflection coefficient in dB (S_{11})

(b) Forward gain in dB (S_{21})

Figure 4.6: Scattering parameters

4.5 Antenna Assembly

A quarter-wavelength impedance transformer was milled using the ProtoMat S63 PCB milling machine for each antenna. Figure 4.7 shows the impedance matching network on FR-4. This needed to be physically and electrically connected to the antenna element on

Lexan. Due to the difference in thickness between the FR-4 material and the Lexan material,

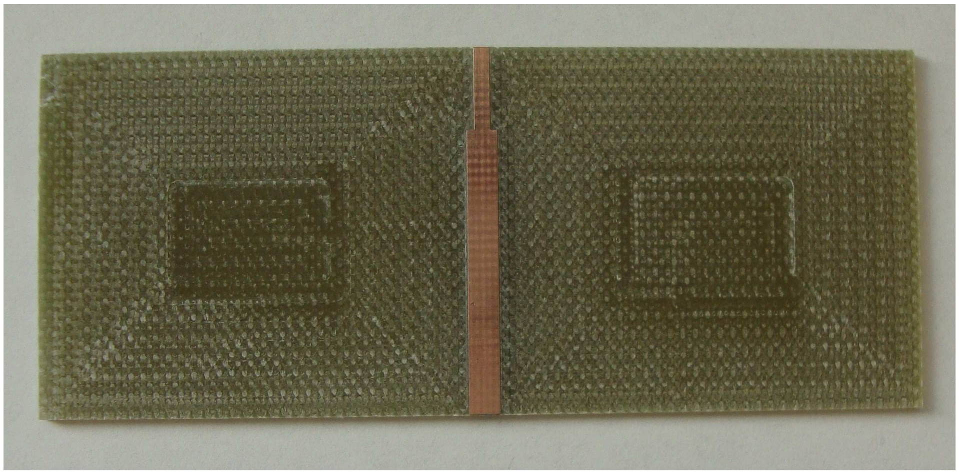

Figure 4.7: Quarter-wavelength impedance transformer on FR-4

an aluminum shim was adhered to the ground plane of the FR-4 material making the total thickness comparable to the thickness of the Lexan. Next the FR-4 material was adhered to the Lexan, and the quarter-wavelength impedance transformer's transmission line was electrically connected to the feed line for the antenna by means of copper tape with an electrically conductive adhesive. Additionally, the antenna's ground plane was electrically connected to the ground plane on the FR-4 material using the same copper tape with an electrically conductive adhesive. For this connection, the copper tape strips overlapped in order to form one continuous conductor. Figure 4.8a shows the copper foil ground plane for the resonator electrically connected to the ground plane of the FR-4 material. Lastly, the SMA connector was soldered to the FR-4 material. Figure 4.8 shows the top and bottom of the solid copper antenna with a solid copper ground plane.

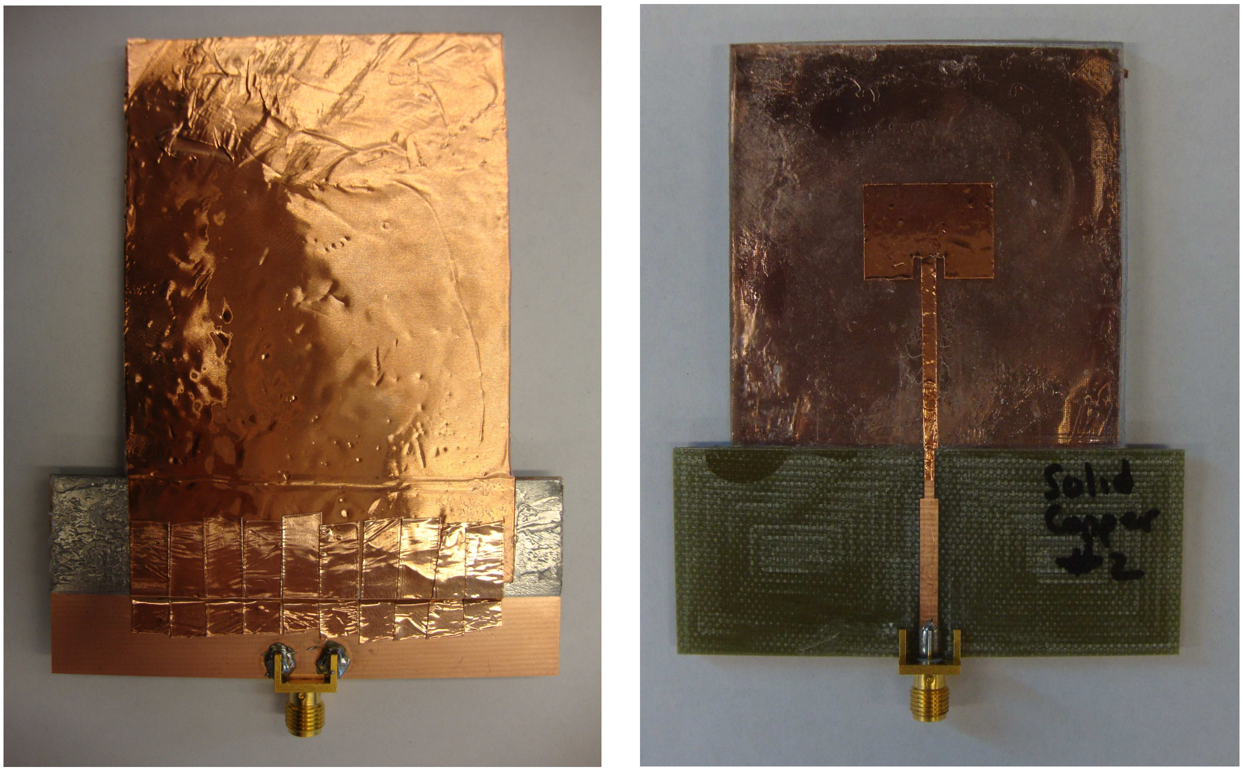

(a) Bottom side of antenna

(b) Top side of antenna

Figure 4.8: Fabricated solid copper antenna over a solid copper ground plane

The performance of the fabricated antennas was measured with a vector network analyzer (VNA) as well as a far-field anechoic chamber. The setup and calibration procedure for the anechoic chamber is outlined in Appendix B. The next chapter discusses the results obtained from the empirical measurements.

CHAPTER 5

Empirical Results

5.1 Introduction

In this chapter, the empirical measurements for the fabricated antennas are presented. The antennas were fabricated using the technique outlined in Chapter 4. The performance metrics used to analyze the antennas includes the scattering parameters, antenna gain, and the radiation patterns. The scattering parameters are used to determine the frequencies at which the antenna is resonant, whereas the radiation pattern is used to show spatially where the antenna is radiating.

5.2 Measurement Setup

The equipment used to measure the antenna's performance includes a vector network analyzer (VNA) as well as the combination of a vector signal generator and signal analyzer. While the antenna's scattering parameters were measured using the VNA, the antenna's gain and radiation patterns were measured in an anechoic chamber using the vector signal generator and signal analyzer. The VNA was easily calibrated using an Ecal module. However, obtaining dBi measurements in the anechoic chamber required a more involved procedure. In Appendix B, the procedure taken to calibrate the anechoic chamber is outlined and explained.

To understand the performance of an antenna composed of optically transparent mesh material, it is compared to the performance of an antenna composed of solid copper. The first set of antennas fabricated included an optically transparent resonator over a solid copper ground plane as well as a solid copper resonator over a solid copper ground plane. After the performance of these two antennas was measured, the solid copper ground planes were removed and replaced with the optically transparent mesh material, and the performance of the second set of antennas was measured. Images for all four antennas can be found in Appendix A. This measurement campaign kept the resonator as a control while the ground plane material changed. This allowed the influence of the mesh material to be observed. Additionally, the performance of the solid copper and optically transparent resonators can be compared. However, each resonator was cut independently by hand and therefore there are differences in the dimensions.

5.3 Scattering Parameters

The first performance metrics analyzed were the scattering parameters of the antennas. The scattering parameters describe an input-output path of a system, and the reflection coefficient (S_{11}) measurement shows how much energy is reflected back to the generator. This is important to understand because a significant amount of energy reflected back means less energy is transmitted and the device is not efficient, and secondly, the large amounts of reflected energy can damage various components, such as amplifiers. The performance of all four antennas are tabulated for comparison in Table 5.1.

5.3.1 Solid Copper Resonator

Figure 5.1 compares the reflection coefficient measured for the solid copper resonator with both ground planes, solid and mesh. For assistance with observing the antenna's resonance, a dotted line has been added at the -10 dB point.

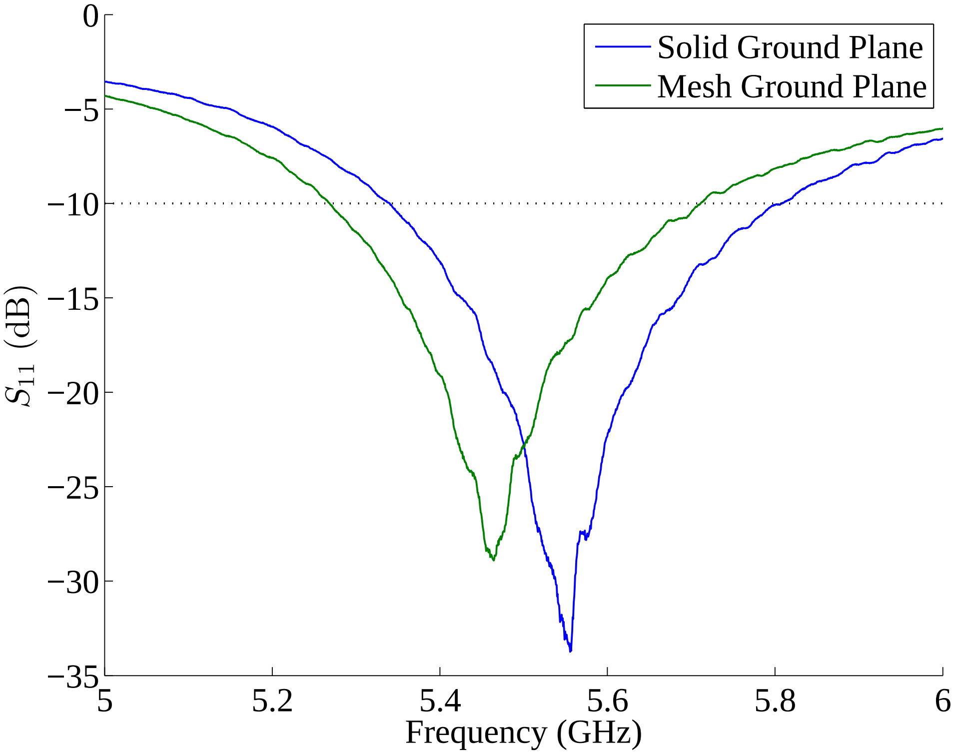

Figure 5.1: Solid copper resonator (S_{11})

For both ground planes, the solid copper antenna had a very distinct resonance. With the solid copper ground plane, a 10 dB return loss bandwidth of 8.2% centered at 5.55 GHz was achieved, while a 8.0% bandwidth centered at 5.46 GHz was achieved with the optically transparent mesh ground plane. The maximum return loss for the two antennas was 33.74 dB and 28.82 dB respectively for the solid copper ground plane and the optically transparent ground plane. A high return loss means less energy is reflected back to the generator. This is important to ensure various RF equipment and components, such as amplifiers, will not be damaged.

5.3.2 Optically Transparent Resonator

Figure 5.2 compares the reflection coefficient measured for the optically transparent resonator with both ground planes, solid and mesh. For assistance with observing the antenna's resonance, a dotted line has been added at the -10 dB point.

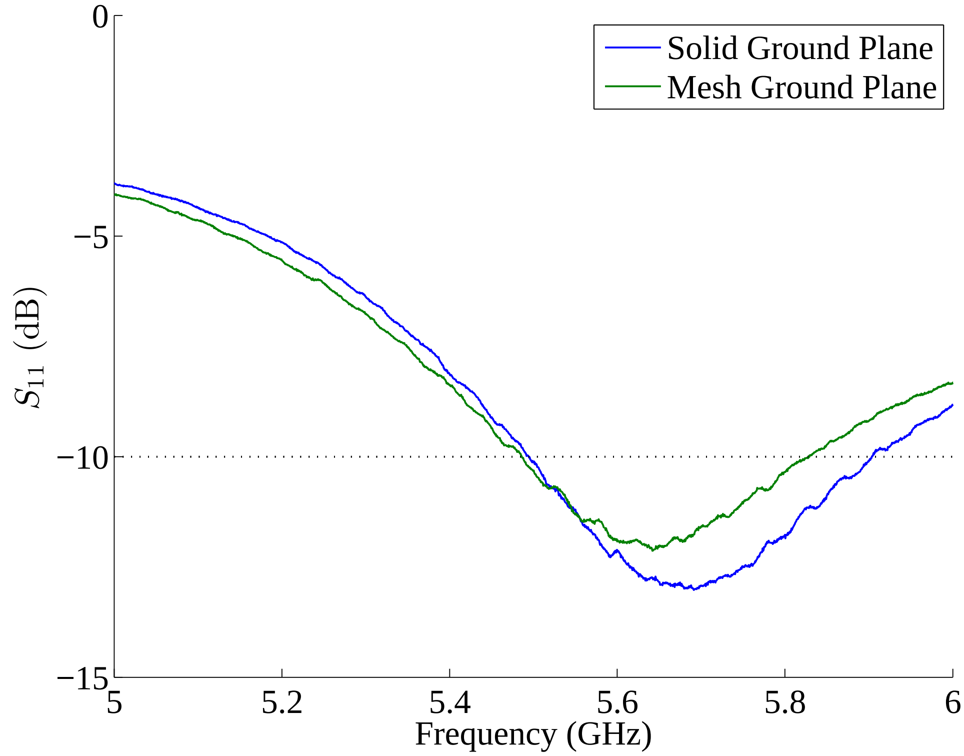

Figure 5.2: Optically transparent resonator (S_{11})

With a solid copper ground plane, a 10 dB return loss bandwidth of 7.1% centered at 5.69 GHz was achieved, while a 6.1% bandwidth centered at 5.64 GHz was achieved with the optically transparent mesh ground plane. Additionally, a maximum return loss of 13.03 dB and 12.14 dB were achieved for the solid copper ground plane and optically transparent mesh ground plane, respectively. The same is true for the mesh resonator as for the solid copper resonator. The performance of the antenna with a solid copper ground plane is better than the performance of the antenna with an optically transparent ground plane, which is expected due to the higher ohmic losses associated with the mesh material.

5.3.3 Performance comparison for both resonators

The prior sections showed the how the mesh material impacted the performance of either the solid copper or optically transparent resonator. It is also important to understand how the performance of the two resonators compare. Table 5.1 shows the performance for all four antennas based on the measured scattering parameters. The results show both antennas are resonating in the 5 to 6 GHz frequency band. However, the performance of the solid copper resonator is superior to the performance of the optically transparent mesh resonator. The most notable difference in the performance of the mesh resonator to the copper resonator is the maximum return loss. For both ground plane configurations, the solid copper resonators maximum return loss is more than double that of the optically transparent resonator. Both resonators were cut by hand using a jig which was precisely milled to the proper dimensions, and these results suggest the mesh material has a higher

	Solid Copper Resonator		Transparent Mesh Resonator	
	Solid Copper Ground Plane	Transparent Mesh Ground Plane	Solid Copper Ground Plane	Transparent Mesh Ground Plane
Center Freq. f_c (GHz)	5.55	5.46	5.69	5.64
Bandwidth (% of f_c)	8.2	8.0	7.1	6.1
Max. Return Loss (dB)	33.74	28.82	13.03	12.14

Table 5.1: Performance of fabricated antennas based on scattering parameters

sensitivity to inaccurate dimensions. This is expected because of the realizable dimension limitation of the mesh material. This affects the dimension of the antenna as well as the feeding network. These effects are discussed further in the next section where the simulated antennas are compared to the fabricated antennas.

5.3.4 Compare Empirical and Simulated Performance

In addition to comparing the two sets of fabricated antennas together, the measured scattering parameters of the two antennas with the solid copper ground plane are compared to the two antennas simulated in HFSS.

Since the antennas were simulated with a solid copper ground plane, the performance of the simulated antennas is compared to the performance of the fabricated antennas with a solid copper ground plane. Figure 5.3 shows the plot of the scattering parameters for the fabricated and simulated antennas. It is clear that the fabricated optically transparent mesh antenna's performance is inferior to the performance of the simulated antenna. This dis-

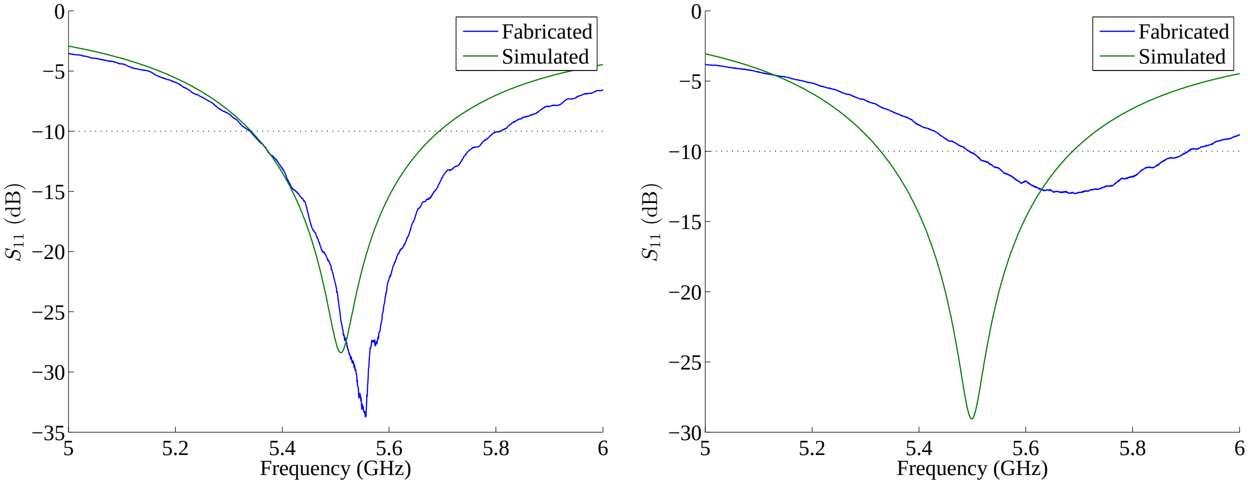

(a) Solid copper resonator

(b) Optically transparent resonator

Figure 5.3: Compare fabricated and simulated scattering parameters

crepancy can largely be attributed to the fabrication procedure as well as material property variations. Since the resonators for these antennas were cut by hand, it is a safe assumption that the optically transparent antenna does not contain a continuous conductive strip on the outside edges, which greatly affects the transmission line width as well as the inset feed dimensions. As a result, the proper match is lost, and the magnitude of the reflection coefficient increases. In contrast however, the fabricated solid copper antenna's performance is very similar to the performance of the simulated solid copper antenna. The fabricated antennas underwent a resonant frequency shift, which can be explained by slight variations in the patch antenna's dimensions. It was shown in Figure 4.1 that sub-millimeter variations in the patch antenna's length causes a shift in the resonant frequency. These results suggest the mesh material is more sensitive to inaccurate dimensions, which is expected since there are a discrete set of realizable dimensions which can be used based on the mesh material geometry. These discrepancies however, may be ameliorated through a more robust fabrication procedure, such as photolithography, or a less complex process such as utilizing a steel rule die. These would ensure the resonators were more precisely cut to the necessary dimensions.

5.4 Antenna Gain

In addition to the scattering parameters, analyzing the the gain of the antenna over a frequency range also shows what frequencies the antenna functions over. The gain for each antenna was measured in the anechoic chamber over the 5 to 6 GHz frequency range in 50 MHz increments. The antenna's performance is presented for the individual resonators as a function of the ground plane, and Table 5.2 tabulates the performance of all four antennas.

5.4.1 Solid Copper Resonator

Figure 5.4 presents the gain of the solid copper resonator over a solid copper, and an optically transparent mesh, ground plane. While a peak gain of 8.09 dBi at 5.75 GHz was achieved with a solid copper ground plane, a peak gain of 7.1 dBi at 5.6 GHz was achieved with the optically transparent mesh ground plane. The fact that the peak gain of the antenna with the optically transparent ground plane is lower than the peak gain of the antenna with the solid copper ground plane is in agreement with the scattering parameters presented in the prior section. Since the sheet resistance of the optically transparent mesh material is higher than the solid copper there is a greater ohmic loss and thus a reduced gain. Additionally, with a mesh ground plane there is more energy radiating through the ground plane [14], which results in a lower peak gain.

In addition to peak gain, a common performance metric used to determine the range of frequencies over which the antenna functions is found using the -3 dB point from the peak gain. Using this criteria, the antenna with a solid copper ground plane functions over the range 5.3 to 5.95 GHz, while the antenna with an optically transparent mesh ground plane functions over the range 5.25 to 5.95 GHz. The center frequencies for these two ranges were determined by averaging the upper and lower frequency bounds. Using the gain of the antenna, the bandwidth for the solid copper antenna with a solid copper ground plane was calculated to be 11.6% centered at 5.625 GHz, and a bandwidth of 12.5% centered at 5.6 GHz was calculated for a optically transparent mesh ground plane. These results are larger than what was calculated from the scattering parameters. However, the scattering parameters are a benchmark measurement as they are performed in the lab room, whereas the gain measurements are performed using an anechoic chamber where there is no interference from

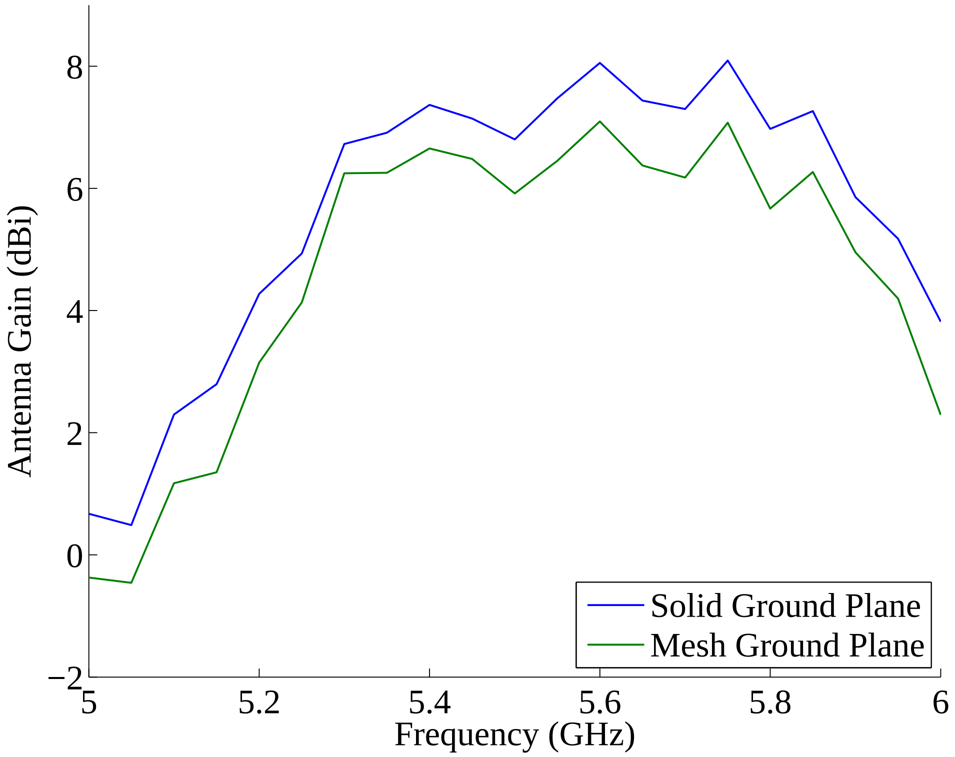

Figure 5.4: Solid copper resonator gain (dBi)

other signals, or reflected waves.

5.4.2 Optically Transparent Resonator

Figure 5.5 presents the gain of the optically transparent mesh resonator over solid copper, and optically transparent mesh, ground planes. A peak gain of 5.73 dBi at 5.6 GHz was achieved with the solid copper ground plane, and a peak gain of 5.55 dBi at 5.6 GHz was achieved with the optically transparent mesh ground plane. Similar to the case of the solid copper resonator, the peak gain achieved with the solid copper ground plane is higher than the peak gain achieved with the optically transparent mesh ground plane. This result is in agreement with the scattering parameter measurements: the lower the return loss, the less energy can be radiated from the antenna.

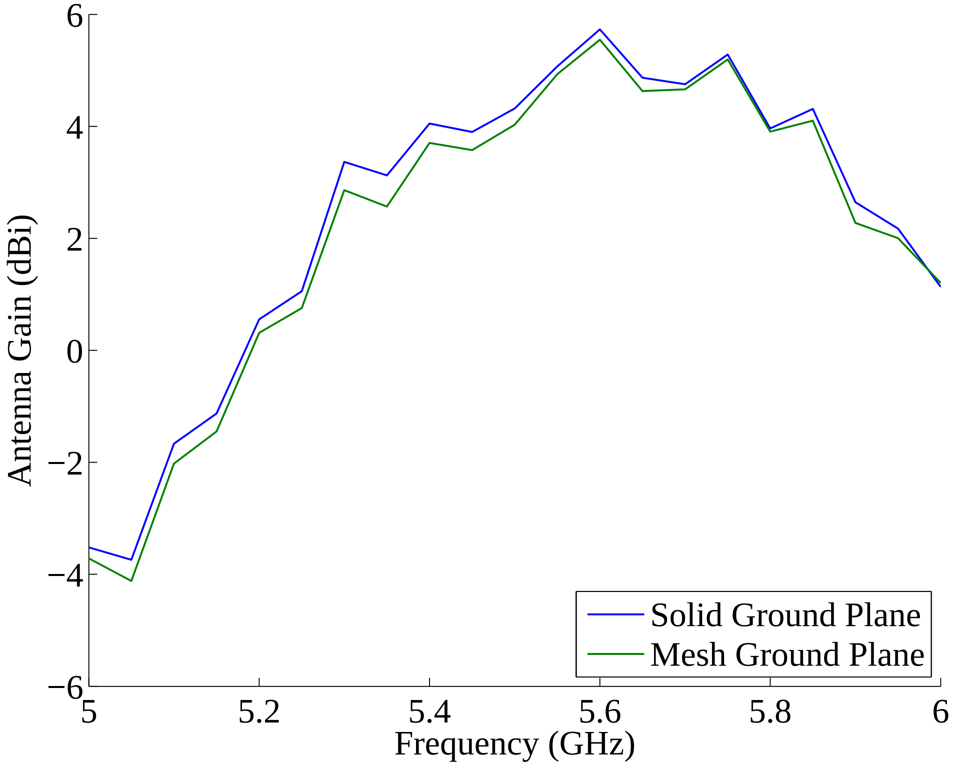

Figure 5.5: Optically transparent resonator gain (dBi)

Using the -3 dB criteria, the optically transparent resonator functions over the frequency range 5.3 to 5.9 GHz with a solid copper ground plane, and 5.3 to 5.85 GHz with an optically transparent mesh ground plane. From these ranges, a bandwidth of 10.7% centered at 5.6 GHz and 9.9% centered at 5.575 GHz were calculated. Similar to the case with the solid copper resonator, the bandwidths calculated with the -3 dB criteria are larger than the bandwidths calculated with the scattering parameters.

5.4.3 Performance comparison for both ground planes

The prior sections showed how the mesh material, when used as the ground plane, impacted the gain of an antenna. In this section, the performance of the two resonators are compared to show the impact of using mesh material for the resonator. The gains of all four antennas are tabulated in Table 5.2 for comparison.

	Solid Copper Resonator		Transparent Mesh Resonator	
	Solid Copper Ground Plane	Transparent Mesh Ground Plane	Solid Copper Ground Plane	Transparent Mesh Ground Plane
Peak Gain (dBi)	8.09	7.1	5.73	5.55
Frequency at Peak Gain (GHz)	5.75	5.6	5.6	5.6
-3 dB Range (GHz)	5.3 to 5.95	5.25 to 5.95	5.3 to 5.9	5.3 to 5.85
Bandwidth (From -3 dB)	11.6%	12.5%	10.7%	9.9%

Table 5.2: Performance of fabricated antennas based on antenna gain

When using the optically transparent mesh material as the resonator, the gain could suffer due to losses associated with the higher sheet resistance of the mesh material. However, the bandwidths for the solid copper and optically transparent resonators are comparable. This supports the concept that the optically transparent mesh material can be used instead of solid copper for an antenna.

5.5 Radiation Patterns

The last performance metric analyzed is the radiation pattern of the antennas. The radiation pattern shows the gain of the antenna as a function of direction. Each antenna's radiation pattern was measured in the far-field anechoic chamber at the frequency of the peak gain, f_{peak}, as well as the center frequency, f_c, based on the scattering parameters. For each radiation pattern, the antenna's beamwidth was calculated. The beamwidth is used to describe the area over which an antenna receives and transmits a signal. The beamwidth also describes how directive an antenna is. The narrower the beamwidth the more directive the antenna, and in contrast the wider the antenna's beamwidth, the less directive it is.

For all radiation patterns plotted, the patch element is oriented such that 0° is normal to the top surface of the patch element, and the azimuthal radiation plane is mapped in the direction of the patch elements width, see Figure 5.6.

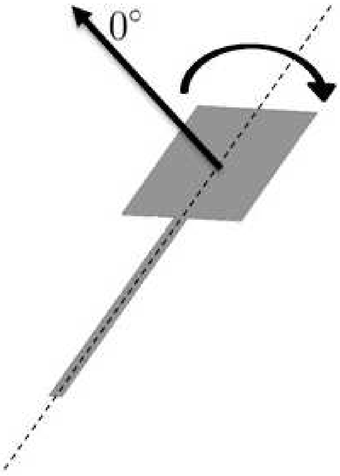

Figure 5.6: Orientation of patch antenna for radiation pattern measurements

5.5.1 Solid Copper Resonator

Figure 5.7 presents the azimuthal plane radiation patterns of the solid copper resonator over solid copper, and optically transparent mesh ground planes. Operating at the antenna's center frequency (5.55 GHz), the solid copper resonator over a solid copper ground plane achieved a beamwidth of 65°, while a beamwidth of 70° was achieved when operating at the peak gain frequency (5.75 GHz). With an optically transparent ground plane, a beamwidth of 65° was achieved when operating at the antenna's center frequency (5.45 GHz) as well as the peak gain frequency (5.6 GHz). These measurements are all very close, as expected, the ohmic losses caused by the mesh material would not alter the antenna's directivity.

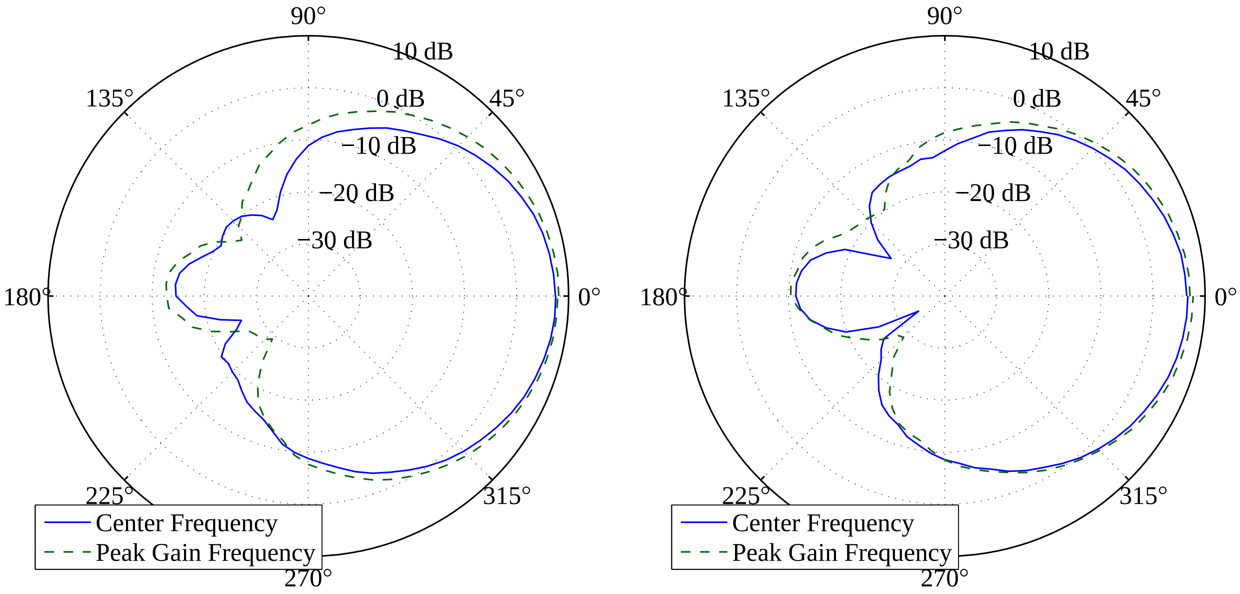

(a) Solid copper ground plane

(b) Optically transparent ground plane

Figure 5.7: Radiation pattern for antennas solid copper resonator

5.5.2 Optically Transparent Resonator

Figure 5.8 presents the azimuthal plane radiation patterns of the optically transparent mesh resonator over solid copper, and optically transparent mesh ground planes. With the solid copper ground plane, a beamwidth of 75° was achieved when operating at the center frequency (5.7 GHz), and a beamwidth of 65° was achieved when operating at the peak gain frequency (5.6 GHz). When the solid copper ground plane was replaced with the optically transparent mesh material, a beamwidth of 65° was achieved when operating at the antenna's center frequency (5.65 GHz) as well as the peak gain frequency (5.6 GHz). Similar to the case of the solid copper resonator antennas, the beamwidths are all very close in value. The largest difference is 10°, which could be attributed to measurement error. Additionally, since the radiation pattern measurement was quantized into five degree increments, there is an

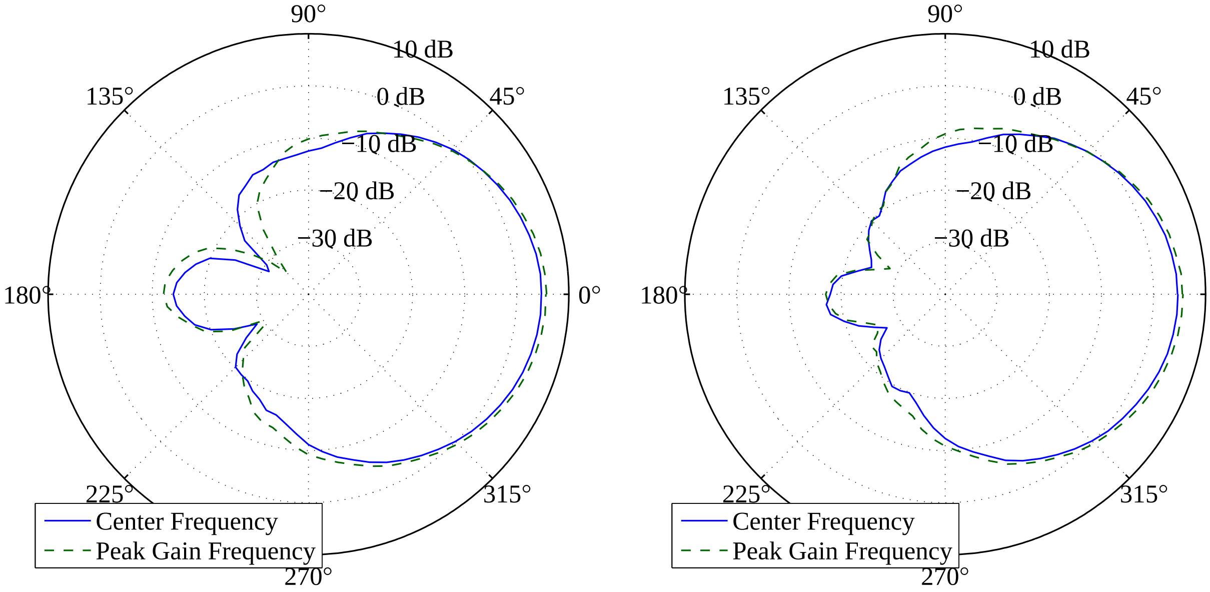

(a) Solid copper ground plane

(b) Optically transparent ground plane

Figure 5.8: Radiation pattern for optically transparent resonator

uncertainty of two and a half degrees in the measurement.

5.5.3 Performance comparison for both ground planes

The prior sections illustrated that the optically transparent mesh material, when used as the ground plane, did not significantly affect the performance of the antenna as compared to an identical antenna with a solid copper ground plane. In this section, the performance of the optically transparent and solid copper resonators are compared.

Table 5.3 shows the performance of all four antennas based on radiation patterns. The majority of the beamwidths measured were 65°, which shows that the mesh material, when used as the resonator and/or ground plane, does not have much of an effect on the antenna's performance.

	Solid Copper Resonator		Transparent Mesh Resonator	
	Solid Copper Ground Plane	Transparent Mesh Ground Plane	Solid Copper Ground Plane	Transparent Mesh Ground Plane
Beamwidth (f_c)	65° (5.55 GHz)	65° (5.45 GHz)	75° (5.7 GHz)	65° (5.65 GHz)
Beamwidth (f_{peak})	70° (5.75 GHz)	65° (5.6 GHz)	65° (5.6 GHz)	65° (5.6 GHz)

Table 5.3: Performance of fabricated antennas based on radiation patterns

Throughout this chapter, the performance of an antenna fabricated from optically transparent mesh material was compared to the performance of an antenna fabricated from solid copper using three different performance metrics. First, the reflection coefficient was presented. These measurements showed the return loss of the antenna remained relatively constant when the resonator was kept as a control while the ground plane material was changed. Additionally, the scattering parameters showed that when the resonator is composed of either solid copper or an optically transparent mesh material, it still achieves a resonance. Second, using the peak gain of the antenna over the desired frequency range, it was shown that there was a 2-3 dB difference between the peak gain achieved with the solid copper antenna and the optically transparent antenna. Additionally, the peak gain showed the frequency range over which the optically transparent and solid copper antennas function was nearly the same with about a 50 MHz difference. Lastly, the radiation patterns showed both antennas radiate energy in the same directions. The above performance analysis proves optically transparent mesh material can be used to fabricate a microstrip patch antenna element. The next chapter discusses the feasibility of utilizing an optically transparent antenna array for beamforming and beamsteering applications.

CHAPTER 6

Dual-Polarized Antenna Array

6.1 Introduction

With the performance of a single element optically transparent antenna verified, the next step was to analyze an optically transparent array. Previous work included a simulation-based analysis of an antenna array composed of dual-polarized optically transparent microstrip patch elements [44]. In this chapter, the development of a dual polarized optically transparent antenna array is outlined, starting with the validation of a single element by comparing the performance of an optically transparent single element to the performance of a solid copper element, to simulating and validating an eight-element uniform linear array (ULA). This analysis was performed using the ANSYS® High Frequency Structure Simulator (HFSS) software package. The work presented in this chapter was published and presented in Progress In Electromagnetics Research Symposium (PIERS) in Stockholm, Sweden in 2013.

6.2 Single-Element Dual-Polarized Design

For mesh material geometries, there is a tradeoff between optical transparency and realizable dimensions based on the mesh line width, q, and pitch, p. Pitch dimensions of 100, 200, and 300 μm have been previously considered [15]. Figure 6.1 shows the geometry of the dual-polarized optically transparent microstrip patch antenna with a mesh line width of 20 μm and a pitch of 200 μm. This geometry was chosen as a balance between transparency, conductivity, and manufacturability. The dielectric material used was polyethylene terephalate, PET ($\epsilon_r = 2.6$). With this configuration and a material thickness of 35 μm, an optical transparency of 82.6% and electrical conductivity of 1.205×10^7 S/m were achieved. The mesh material introduced an excessive number of objects in the HFSS simulation, and prior work has shown that a mesh behaves like a solid piece of copper. Therefore, the mesh material was approximated by a solid conducting element with a bulk conductivity of 1.205×10^7 S/m, for a feasibility simulation-based study.

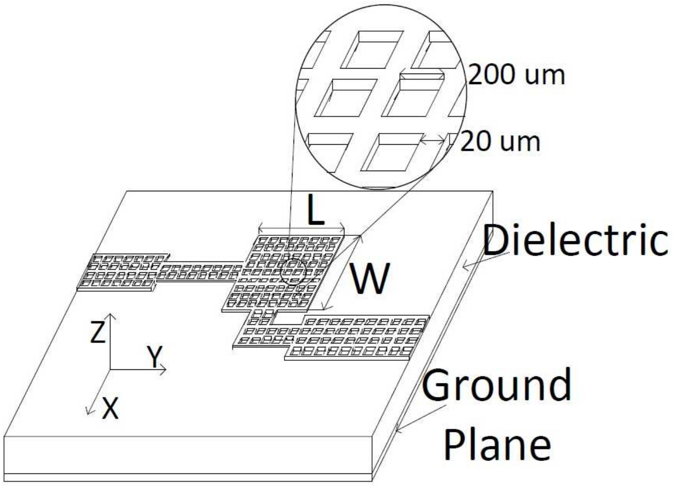

Figure 6.1: Dual polarized single element antenna

The initial design for the microstrip patch antenna was done using the equations presented in Section 2.3.1. With the operating parameter values presented in Table 6.1, the length and width of the antenna were calculated to be 14.91 mm and 20.33 mm respectively.

ϵ_r	2.6
f_r	5.5 GHz
h	3.3 mm

Table 6.1: Patch antenna operating parameter values

Since this antenna design was for a dual polarized patch antenna, the length and width needed to be the same, $L = W$, in order to have the same resonant frequency for both polarizations. Therefore, using HFSS, the dimensions of the antenna were tuned such that a square patch element resonated properly at 5.5 GHz. The length and width of the properly tuned patch antenna were both 14.76 mm. A solid copper antenna was simulated with the same dimensions as the mesh antenna, as seen in Figure 6.1, to compare performance. In this simulation, the optically transparent mesh material was approximated by a solid conducting material, and therefore the realizable dimensions achievable by the mesh material were not taken into account [44].

6.2.1 Feeding Network

The radiating element, as shown in Figure 6.1, is composed of a patch antenna and two feeding networks, one for each polarization. The feeding network included a 50 Ω transmission line and a quarter-wavelength impedance transformer, to match the 50 Ω transmission line to the patch antenna. Through HFSS simulations, the resonant input impedance for the pure copper antenna and the approximated optically transparent antenna was determined to be 290.1 Ω and 290.7 Ω respectively. Since the two resonant input impedances were nearly equal, a single quarter-wavelength impedance transformer was designed and used for both antennas.

The design procedure was followed as outlined in Section 2.3.2.1, with the desired input impedance, Z_{in}, equal to the characteristic impedance of the transmission line, 50 Ω, and the load impedance, Z_L, equal to the resonant input impedance of the patch, 290.7 Ω. Using Equation 2.18, the characteristic impedance for the quarter-wavelength impedance transformer was calculated to be 120.5 Ω. Each microstrip transmission line was designed based on the physical and electromagnetic properties of the PET substrate as well as the desired characteristic impedance. Using transmission line theory equations presented in Appendix C, the widths of the 50 Ω and the 120.5 Ω transmission lines were calculated to be 9.18 mm, 1.589 mm respectively. Additionally, the length of the quarter-wave impedance transformer was calculated to be 9.82 mm.

6.2.2 Scattering Parameters

The first performance metric presented for the single element antenna is the reflection coefficient (S_{11}). Figure 6.2 shows the magnitude of the reflection coefficient in dB for the input port for both polarization feeds. Using Figure 6.1 as reference, the vertically polarized excitation is feedline to the patch in the y-axis, whereas the horzontally polarized excitation is the feedline to the patch in the x-axis. Additionally, when one polarization feed is used to excite the patch antenna, the other feed is terminated with a matched load. For the mesh antenna element, a bandwidth of 4.1% with a center frequency of 5.48 GHz is achieved when vertically excited, whereas the horizontally polarized excitation has a 4.9% bandwidth with a center frequency of 5.515 GHz. This performance is comparable to the solid copper antenna element, which achieved a bandwidth of 4% with a center frequency of 5.495 GHz when excited with the vertically polarized feed, and a bandwidth of 4.8% with a center frequency of 5.525 GHz when excited with the horizontally polarized feed. The reflection coefficient, S_{11}, shows at which frequencies the antenna is resonating because it is a measure of how much energy is reflected back to the transmitter. Therefore, if the return loss is greater than 10 dB, then less than 10% of the power transmitted is reflected back. The bandwidth measurement shows the frequencies over which this occurs.

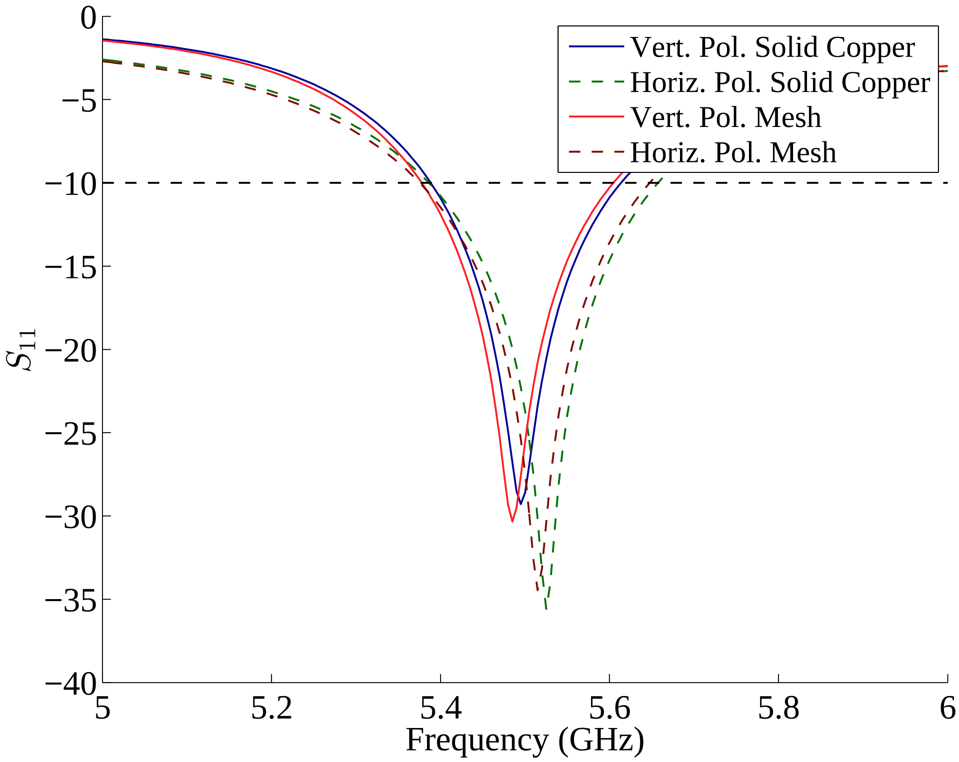

Figure 6.2: Magnitude of reflection coefficient (S_{11}) in dB

6.2.3 Radiation Pattern

In addition to the reflection coefficient, the radiation pattern for the single element was simulated. While the S_{11} was used to determine the frequencies over which the antenna was resonant, the radiation pattern is used to determine where the power is being radiated spatially. Since the antenna array will be steered in the azimuthal plane, only the azimuthal plane radiation pattern is presented for the single element (see Figure 6.3). When the mesh antenna element is vertically polarized, a beamwidth of 140° is achieved, whereas a beamwidth of 62° is achieved when horizontally polarized. This performance is very similar to the solid copper antenna element, which achieves a 120° beamwidth when vertically polarized, and a 66° beamwidth when horizontally polarized.

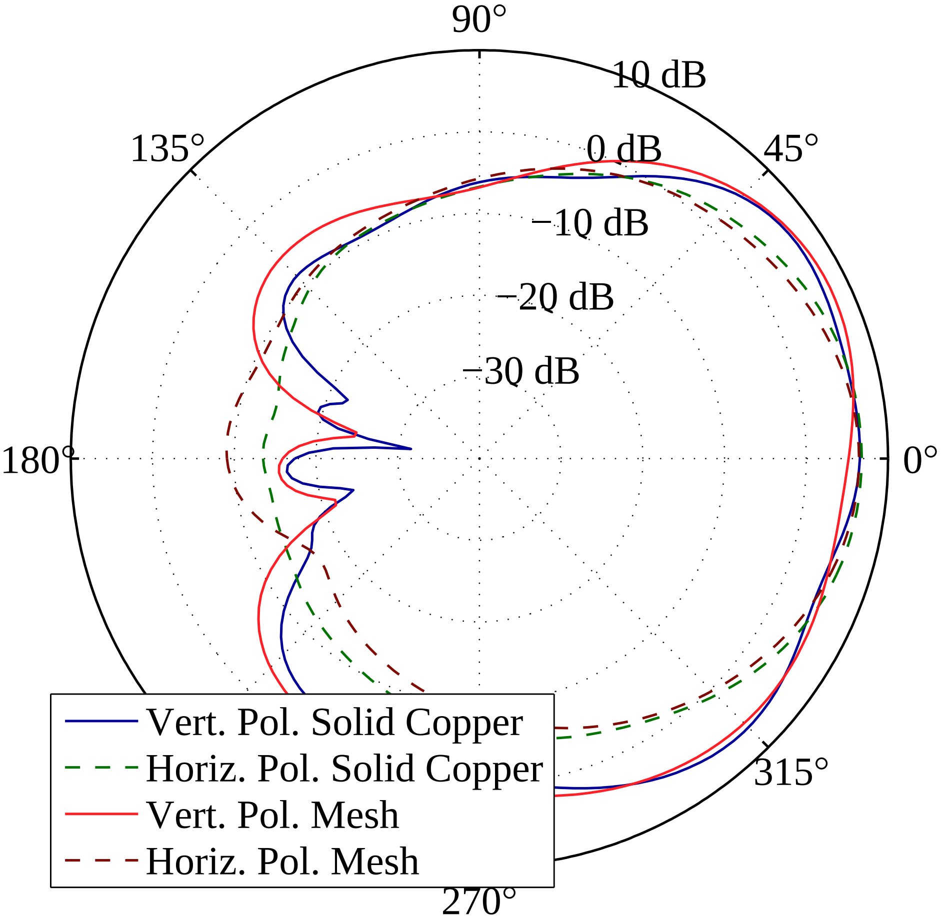

Figure 6.3: Azimuthal plane radiation pattern

These results suggest that mutual coupling occurs between the patch and the different feed lines. The dual-polarized patch antenna requires two different feeds to excite the patch. However, when excited by one polarization, the other feed is still present, causing the radiation pattern to deform. For example, when vertically polarized, the radiation pattern for both the mesh and solid copper antenna elements is stretched in the direction of the other feed line, and the larger beamwidths are achieved.

6.3 Antenna Array

In the previous section, the performance of the single-element dual-polarized optically transparent antenna was shown to be comparable to the performance of a solid copper antenna of the same dimensions. In this section, the performance of an optically transparent antenna array is presented.

In an effort to create a steerable antenna pattern over 120° with a beamwidth of 15°, we chose an eight element array [41]. Figure 6.4 shows the uniform linear array (ULA) of mesh patches with an inter-element spacing of $d = 2.75$ cm, which is $\lambda/2$ at 5.5 GHz.

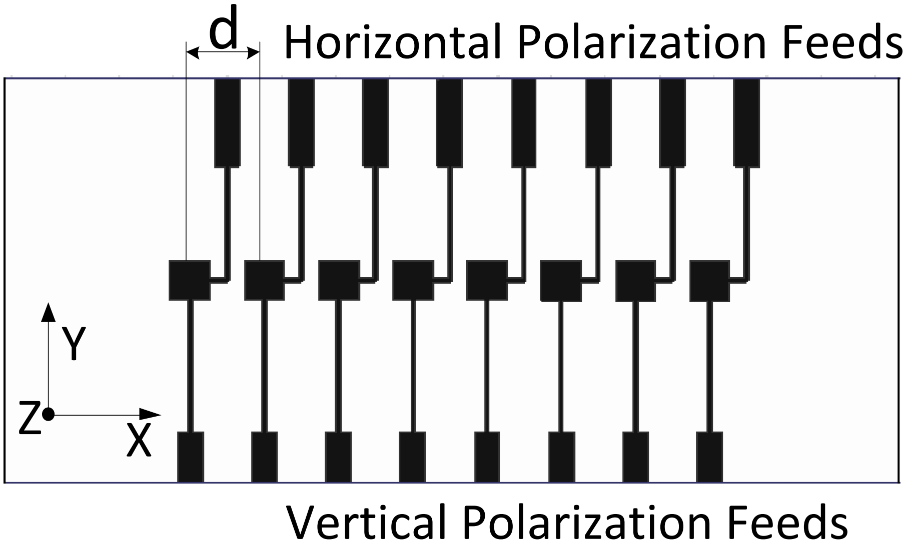

Figure 6.4: Dual polarized eight element array

The performance of the ULA was verified via simulations by shifting the phase of each input port to steer the direction of the main lobe to different angles. Using phased array theory, Equation 2.20, the phase delay of each element was calculated for different steering angles, θ.

6.3.1 Radiation Pattern

The single element performance showed that the mesh material and the solid copper versions behave similarly, therefore the ULA simulation was only performed with the mesh material. In Figure 6.5, the vertically and horizontally polarized azimuthal plane radiation pattern for steering angles $\theta = \{0, 30, 60\}$ degrees are presented. The radiation patterns for steering angles $\theta = \{-30, -60\}$ are symmetric about 0° to the radiation patterns for steering angles $\theta = \{30, 60\}$. These patterns have been omitted in Figure 6.5 in an effort to improve visual clarity. When excited using the horizontally polarized feeds, the peak gain varied between 11.14 to 14.6 dB with a beamwidth varying between 14 to 16°, whereas when the antenna was excited with the vertically polarized feeds, gains between 9.5 and 12.2 dB were achieved, with a beamwidth varying between 14 to 20°. Additionally, the main lobe was at least 7.1 and 2.65 dB greater than the nearest side lobe for the horizontal and vertical polarizations respectively. The lower gain and higher side lobe energy is caused by the mutual coupling between elements. A reduction of the mutual coupling is possible by increasing the inter-element spacing, however this will introduce grating lobes [41].

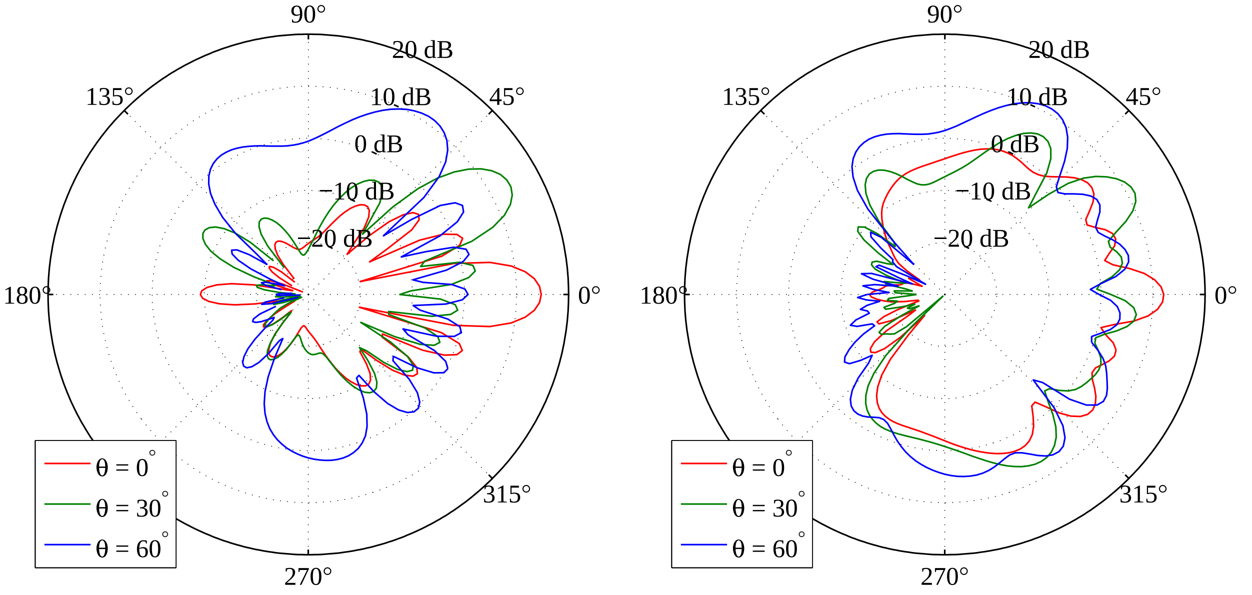

(a) Horizontally polarized (b) Vertically polarized

Figure 6.5: Eight element array radiation pattern

A contribution presented in this chapter was a dual-polarized microstrip patch antenna composed of optically transparent material. Using performance metrics such as scattering parameters as well as radiation patterns, the optically transparent antenna was shown to perform similar to a solid copper antenna of the same dimensions. This simulation-based analysis shows optically transparent mesh material can be used for electrically conducting elements. From this, the second contribution presented in this chapter was the eight-element dual-polarized antenna array. The radiation pattern results proved the optically transparent antenna array was capable of beamsteering through 120° with a beamwidth near 15°. This illuminates the possibility of using optically transparent elements to form an antenna array for beamsteering applications.

CHAPTER 7

Conclusion and Future Work

The main objective of this research was to demonstrate that optically transparent mesh material is a viable material to fabricate antennas. The use of optically transparent material is an attractive avenue for antenna fabrication, as it would produce an antenna which is not only unobtrusive, but easily installed on the inside of windows.

This work showed that there are various challenges associated with the design of a microstrip patch antenna and its feeding network using optically transparent mesh material. The need to maintain realizable dimensions introduces the design challenge of dimension sensitivity. Through a simulation-based analysis, this effect on the performance of two edge-fed feeding mechanisms was compared. Using performance metrics such as scattering parameters and individual antenna radiation patterns, this work showed that the inset feed outperforms the quarter-wavelength impedance transformer.

Using commercially available mesh material, an optically transparent antenna was fabricated and its performance was compared to the performance of a solid copper antenna using performance metrics such as scattering parameters, forward gain, and individual antenna radiation patterns. Through this analysis, the performance of an optically transparent antenna was empirically validated.

Lastly, this work demonstrated the feasibility of employing an optically transparent microstrip patch element in an antenna array. Through phased delay feeding, the radiation pattern was steerable through 120°.

Future work will include physically constructing an array of optically transparent antennas, and measure its beamsteering capabilities. This may require a more robust fabrication procedure since phase delays can be introduced through varying feed line lengths. It is also important to increase the beamwidth of a single patch element. Since the dual polarized antenna array had a peak gain of 14.6 dBi when the steering direction was zero degrees ($\theta = 0°$), and a peak gain of 11.14 dBi when the steering direction was plus or minus sixty degrees ($\theta = \pm 60°$), increasing the beamwidth of the individual patch element will result is a more constant gain over all angles [45].

Bibliography

[1] T. S. Rappaport, *Wireless Communications Principles and Practice.* Pearson Prentice Hall, 2002.

[2] D. Tse and P. Viswanath, *Fundamentals of Wireless Communication.* Cambridge University Press, 2005.

[3] (2015) Cisco visual networking index: Global mobile data traffic forecast update 2014–2019 white paper. [Online]. Available: http://www.cisco.com/c/en/us/solutions/collateral/service-provider/visual-networking-index-vni/white_paper_c11-520862.html

[4] K. Siwiak, *Radiowave Propagation and Antennas for Personal Communications 2nd Edition.* Artech House, Inc., 1998.

[5] (2008) Environmental impacts. File: Cell_phone_tower_disguised_2008.jpg. [Online]. Available: http://en.wikipedia.org/wiki/Mobile_telephony

[6] (2007) Cell antenna concealed to match brick exterior in sopot, poland. File:BTS_NodeB_antenna_Sopot.jpg. [Online]. Available: http://twistedsifter.com/2012/08/examples-of-cell-phone-tower-disguises/

[7] T. Yasin, R. Baktur, and C. Furse, "A comparative study on two types of transparent patch antennas," in *General Assembly and Scientific Symposium, 2011 XXXth URSI*, 2011, pp. 1–4.

[8] J. Saberin and C. Furse, "Challenges with optically transparent patch antennas," *Antennas and Propagation Magazine, IEEE*, vol. 54, no. 3, pp. 10–16, 2012.

[9] H. J. Song, T. Y. Hsu, D. Sievenpiper, H.-P. Hsu, J. Schaffner, and E. Yasan, "A method for improving the efficiency of transparent film antennas," *Antennas and Wireless Propagation Letters, IEEE*, vol. 7, pp. 753–756, 2008.

[10] N. Kirsch, N. Vacirca, E. Plowman, T. Kurzweg, A. K. Fontecchio, and K. Dandekar, "Optically transparent conductive polymer RFID meandering dipole antenna," in *RFID, 2009 IEEE International Conference on*, April 2009, pp. 278–282.

[11] N. Kirsch, N. Vacirca, T. Kurzweg, A. K. Fontecchio, and K. Dandekar, "Performance of transparent conductive polymer antennas in a MIMO ad-hoc network," in *Wireless and Mobile Computing, Networking and Communications (WiMob), 2010 IEEE 6th International Conference on*, Oct 2010, pp. 9–14.

[12] T. Turpin and R. Baktur, “Meshed patch antennas integrated on solar cells,” *Antennas and Wireless Propagation Letters, IEEE*, vol. 8, pp. 693–696, 2009.

[13] T. W. Turpin and R. Baktur, “See-through microstrip antennas and their optimization,” in *Gen. Assemb. Int. Union Radio Sci.*, Aug 2008.

[14] G. Clasen and R. Langley, “Meshed patch antennas,” *Antennas and Propagation, IEEE Transactions on*, vol. 52, no. 6, pp. 1412–1416, 2004.

[15] J. Hautcoeur, F. Colombel, X. Castel, M. Himdi, and E. M. Cruz, “Radiofrequency performances of transparent ultra-wideband antennas,” vol. 22, pp. 259–271, 2011.

[16] J. Hautcoeur, F. Colombel, X. Castel, M. Himdi, and E. Motta Cruz, “Optically transparent monopole antenna with high radiation efficiency manufactured with silver grid layer (AgGL),” *Electronics Letters*, vol. 45, no. 20, pp. 1014–1016, 2009.

[17] C. Mias, C. Tsakonas, N. Prountzos, D. C. Koutsogeorgis, S. C. Liew, C. Oswald, R. Ranson, W. Cranton, and C. Thomas, “Optically transparent microstrip antennas,” in *Antennas for Automotives (Ref. No. 2000/002), IEE Colloquium on*, 2000, pp. 8/1–8/6.

[18] M.-S. Wu and K. Ito, “Basic study on see-through microstrip antennas constructed on a window glass,” in *Antennas and Propagation Society International Symposium, 1992. AP-S. 1992 Digest. Held in Conjuction with: URSI Radio Science Meeting and Nuclear EMP Meeting., IEEE*, vol. 1, June 1992, pp. 499–502.

[19] (2001) S-parameters. [Online]. Available: http://www.microwaves101.com/encyclopedias/438-s-parameters-microwave-encyclopedia-microwaves101-com

[20] R. Ludwig and G. Bogdanov, *RF Circuit Design Theory and Applications.* Pearson Prentice Hall, 2009.

[21] C. A. Balanis, *Advanced Engineering Electromagnetics*, 2nd ed. John Wiley & Sons, 2012.

[22] D. Fleisch, *A Student’s Guide to Maxwell’s Equations.* Cambridge University Press, 2008.

[23] D. M. Pozar, *Microwave Engineering*, 4th ed. John Wiley & Sons, 2012.

[24] (2001) Skin depth. [Online]. Available: http://www.microwaves101.com/encyclopedias/skin-depth

[25] T. Kawashima, H. Matsui, and N. Tanabe, “New transparent conductive films: FTO coated ITO,” *Thin Solid Films*, vol. 445, no. 2, pp. 241–244, 2003.

[26] S.-H. Wei, X. Nie, and S. Zhang, “Electronic structure and doping of p-type transparent conducting oxides,” in *Photovoltaic Specialists Conference, 2002. Conference Record of the Twenty-Ninth IEEE*, May 2002, pp. 496–499.

[27] N. Guan, H. Furuya, K. Himeno, K. Goto, and K. Ito, “A monopole antenna made of a transparent conductive film,” in *Antenna Technology: Small and Smart Antennas Metamaterials and Applications, 2007. IWAT ’07. International Workshop on*, 2007, pp. 263–266.

[28] U. Avachat, F. Yan, D. Metacarpa, and P. Haldar, “Impacts of humidity and temperature on the performance of transparent conducting indium tin oxide and electrical interconnects for solar applications,” in *Photovoltaic Specialists Conference (PVSC), 2013 IEEE 39th*, June 2013, pp. 2983–2986.

[29] N. Guan, H. Furuya, D. Delaune, and K. Ito, “Radiation efficiency of monopole antenna made of a transparent conductive film,” in *Antennas and Propagation Society International Symposium, 2007 IEEE*, June 2007, pp. 221–224.

[30] Sigma-Aldrich. (2015) Indium tin oxide coated glass slide, rectangular. [Online]. Available: http://www.sigmaaldrich.com/catalog/product/aldrich/578274?lang=en&region=US

[31] R. Nagata, Y. Yanagi, S. Fujii, H. Kataura, and Y. Nishioka, “Application of highly conductive DMSO-treated PEDOT:PSS electrodes to flexible organic solar cells,” in *Active-Matrix Flatpanel Displays and Devices (AM-FPD), 2014 21st International Workshop on*, July 2014, pp. 299–302.

[32] J. Nevrela, M. Micjan, M. Novota, S. Flickyngerova, J. Kovac, M. Pavuk, P. Juhasz, J. Jakabovic, and M. Weis, “Technology of conductive polymer PEDOT:PSS films,” in *Advanced Semiconductor Devices Microsystems (ASDAM), 2014 10th International Conference on*, Oct 2014, pp. 1–4.

[33] F. Xue, Y. Su, and K. Varahramyan, “Modified PEDOT-PSS Conducting Polymer as S/D Electrodes for Device Performance Enhancement of P3HT TFTs,” *Electron Devices, IEEE Transactions on*, vol. 52, no. 9, pp. 1982–1987, Sept 2005.

[34] C. Balanis, *Antenna Theory Analysis and Design.* John Wiley & Sons, 2005.

[35] K. R. Carver and J. Mink, “Microstrip antenna technology,” *Antennas and Propagation, IEEE Transactions on*, vol. 29, no. 1, pp. 2–24, Jan 1981.

[36] R. B. Waterhouse, *Microstrip patch antennas: a designer's guide.* Kluwer Academic Publishers, 2003.

[37] R. Waterhouse, D. Novak, A. Nirmalathas, and C. Lim, "Broadband printed sectorized coverage antennas for millimeter-wave wireless applications," *Antennas and Propagation, IEEE Transactions on*, vol. 50, no. 1, pp. 12–16, Jan 2002.

[38] R. Munson, "Conformal microstrip antennas and microstrip phased arrays," *Antennas and Propagation, IEEE Transactions on*, vol. 22, no. 1, pp. 74–78, Jan 1974.

[39] J. Hass, M. Weir, and G. Thomas, *University Calculus.* Pearson Education, Inc., 2007.

[40] R. J. Mailloux, *Phased Array Antenna Handbook.* Artech House, Inc., 2005.

[41] R. Hansen, *Phased Array Antennas.* John Wiley & Sons, 2009.

[42] A. Riley, D. Rascoe, V. Lubecke, J. Huang, and L. Duffy, "Ka-band MMIC beam steered transmitter array," in *Microwave and Millimeter-Wave Monolithic Circuits Symposium, 1989. Digest of Papers., IEEE 1989*, June 1989, pp. 65–68.

[43] (2015) ANSYS HFSS. [Online]. Available: http://www.ansys.com/Products/Simulation+Technology/Electronics/Signal+Integrity/ANSYS+HFSS

[44] E. Escobar, N. Kirsch, and B. Turner, "Antenna array with meshed elemnts for beamforming applications," in *in Progress In Electromagnetics Research*, vol. 1, 2013, pp. 1356–1360.

[45] H. Krim and M. Viberg, "Two decades of array signal processing research: the parametric approach," *Signal Processing Magazine, IEEE*, vol. 13, no. 4, pp. 67–94, 1996.

APPENDICES

APPENDIX A

Fabricated Antennas

In this appendix, images of the fabricated antennas are presented. The fabrication procedure is outline in Chapter 4. The images are outlined as follows:

- Figure A.1 shows the solid copper antenna over a solid copper ground plane
- Figure A.2 shows the optically transparent antenna over a solid copper ground plane
- Figure A.3 shows the solid copper antenna over an optically transparent ground plane
- Figure A.4 shows the optically transparent antenna over an optically transparent ground plane

Figure A.1: Fabricated solid copper antenna over a solid copper ground plane

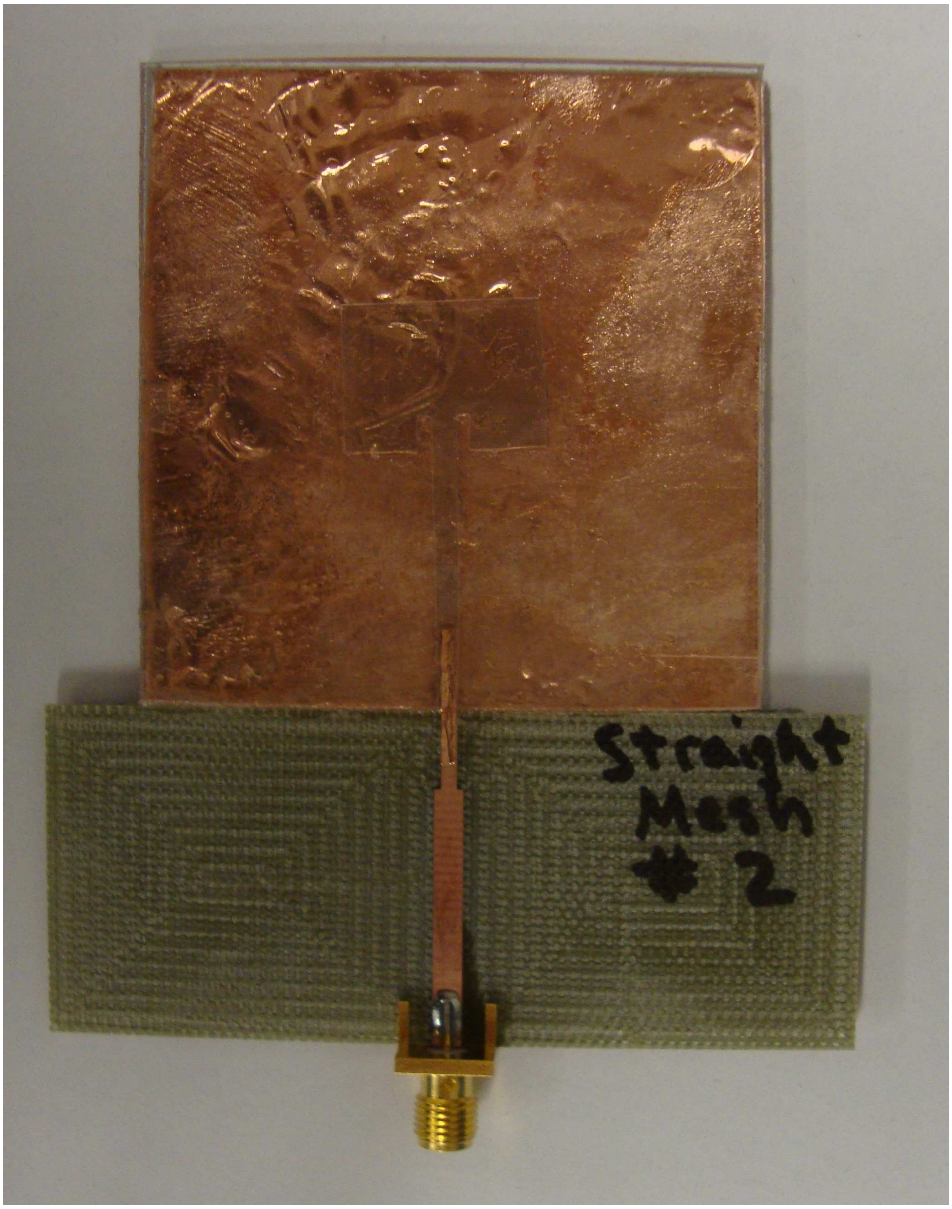

Figure A.2: Fabricated optically transparent antenna over a solid copper ground plane

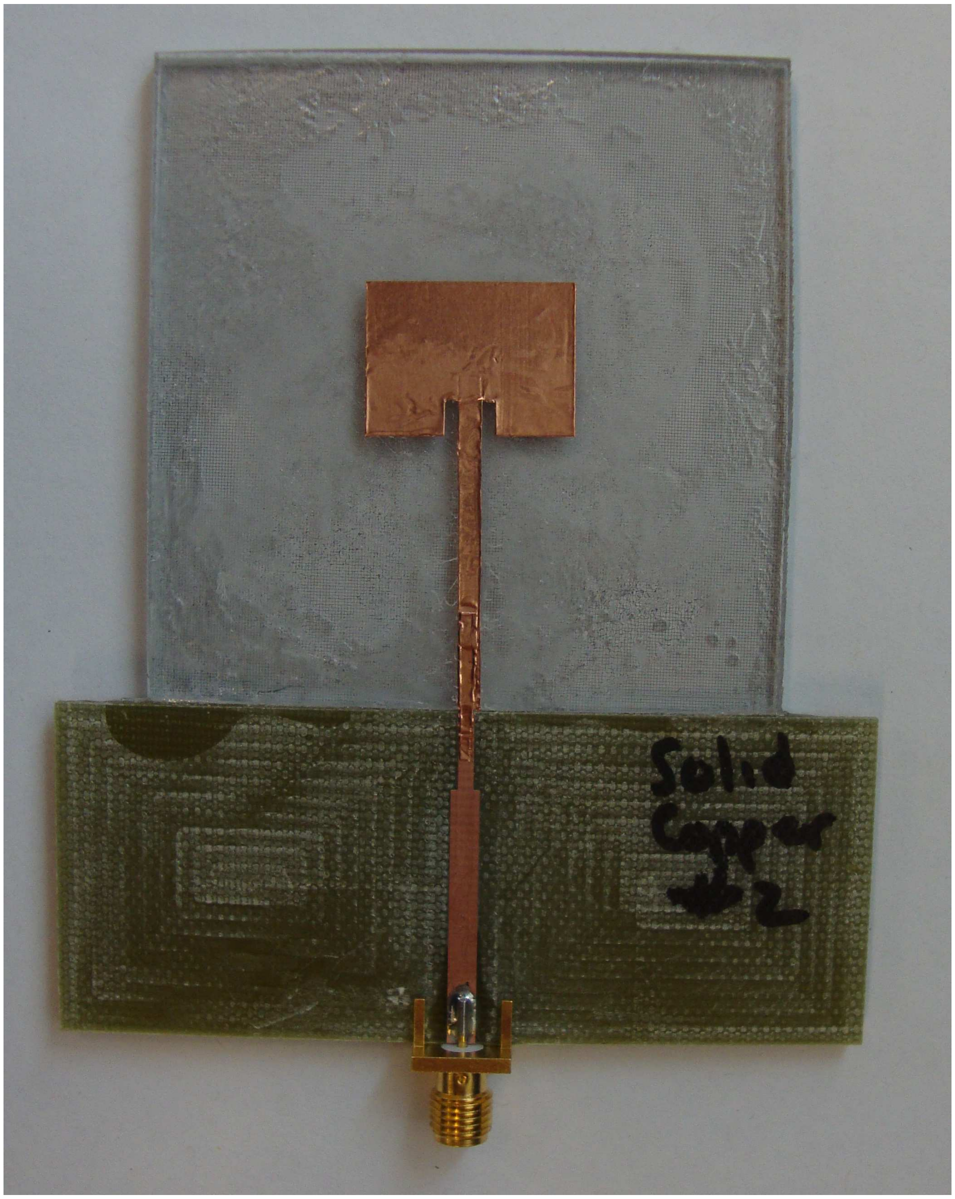

Figure A.3: Fabricated solid copper antenna over an optically transparent ground plane

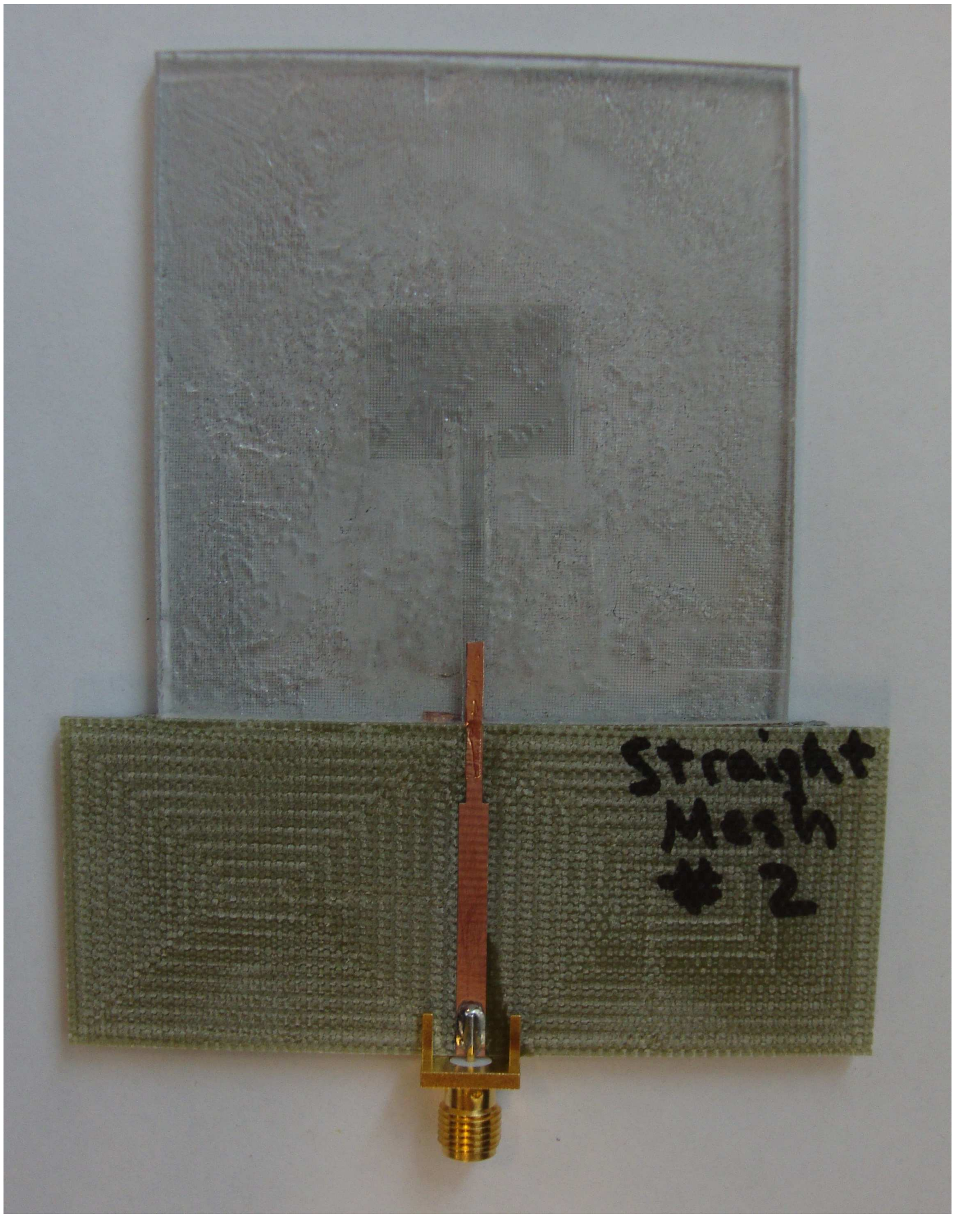

Figure A.4: Fabricated optically transparent antenna over an optically transparent ground plane

APPENDIX B

Anechoic Chamber

Empirical measurements of the antenna's gain were made in a far-field anechoic chamber rated for frequencies in the range 500 MHz to 26 GHz. An anechoic chamber provides isolation from external signals and attenuates internally reflected signals. Shielding Integrity Services Inc. determined the anechoic chamber provided at least 43 dB attenuation of internally reflected signals. In this appendix, the anechoic chamber set up and the calibration process are outline and described.

B.1 Equipment Setup

Outside the anechoic chamber, there are radio frequency (RF) measurement equipment responsible for providing the test signal and measuring the received signal to map the radiation pattern of an antenna. This equipment includes a vector signal generator and a signal analyzer, which are controlled with a computer via Diamond Engineering antenna measurement software. More specifically, the Diamond Engineering Automated Measurement System (DAMS) antenna measurement studio was used.

Inside the anechoic chamber, there is a horn (source) antenna and a positioner. The horn antenna, see Figure B.1a, is connected to a signal generator and is responsible for providing the test signal. It is important to have the horn antenna oriented properly to have the same polarization of the antenna under test (AUT). This antenna is a calibrated antenna, which has a calibration file with known gain values over the frequency range. The positioner, see Figure B.1b, has multiple responsibilities, with the primary duty being the connection and support of the AUT. The AUT connects to the positioner, and a return cable is then connected to the signal analyzer. Additionally, the positioner rotates in the horizontal (azimuthal) and vertical (elevation) planes, allowing the radiation pattern of the AUT to be mapped. The path length between the horn antenna and the positioner is 2.87 m, which is much larger than the far-field distance [1]. Thus all measurement made in the anechoic chamber are far-field measurements.

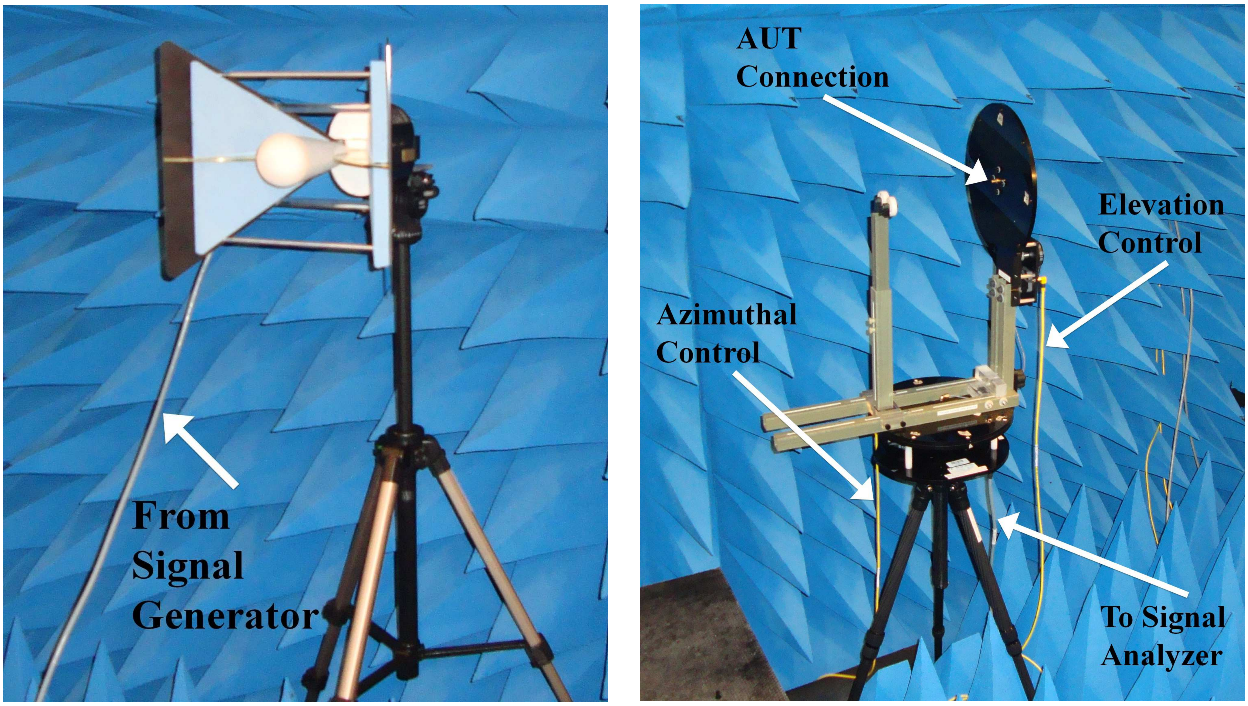

(a) Horn (source) antenna

(b) Positioner apparatus

Figure B.1: Inside the anechoic chamber

Bulkhead adapters are used at the wall of the anechoic chamber to connect the RF measurement equipment to the horn antenna and positioner. In the next section, the calibration procedure for the chamber is described.

B.2 Calibration

Equation B.1 shows the relationship between the received power, transmitted power, and all gains associated with the system. All variables in Equation B.1 are in decibels (dB). The various gains include the gain of the cables G_{Cables}, the gain of the horn (source) antenna $G_{HornAntenna}$, the path gain G_{Path}, and the gain of the antenna under test (AUT) G_{AUT}.

$$P_{Received} = P_{Transmitted} + G_{Cables} + G_{HornAntenna} + G_{Path} + G_{AUT} \tag{B.1}$$

Calculating the gain of the AUT in dBi is done with Equation B.2, once all other gains are known such that they could be calibrated out. The process of measuring or calculating these values are outline in the following sections.

$$G_{AUT} = P_{Received} - (P_{Transmitted} + G_{Cables} + G_{HornAntenna} + G_{Path}) \tag{B.2}$$

B.2.1 Cable Gain

To measure the gain of the cables, the transmitter cable is directly connected to the positioner, see Figure B.2. This configuration removes the gain of the horn antenna, AUT, as well as the path gain from Equation B.1. Algebraically rearranging the remaining terms, the cable gain (G_{Cables}) can be calculated with Equation B.3.

$$G_{Cables} = P_{Transmitted} - P_{Received} \tag{B.3}$$

The signal generator was set to generate a continuous wave at 0 dBm for the desired frequencies, and the power received by the spectrum analyzer was recorded. Figure B.3

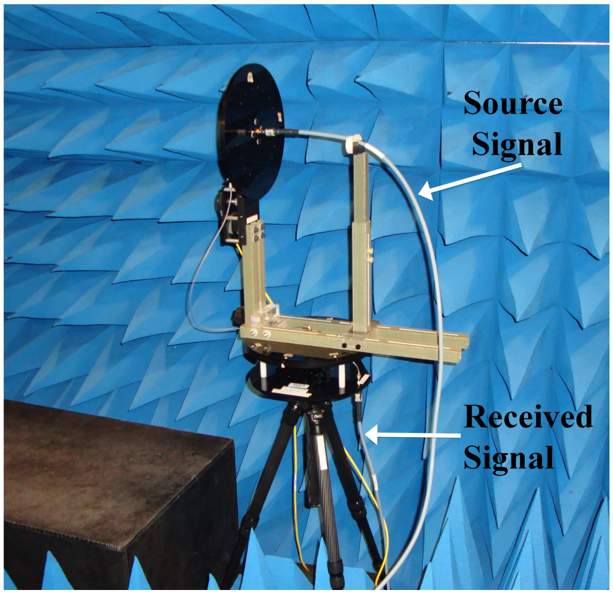

Figure B.2: Cable calibration configuration

shows the gain of the cables over the desired frequency range. There is approximately a 2.5 dB difference between the maximum and minimum gain value.

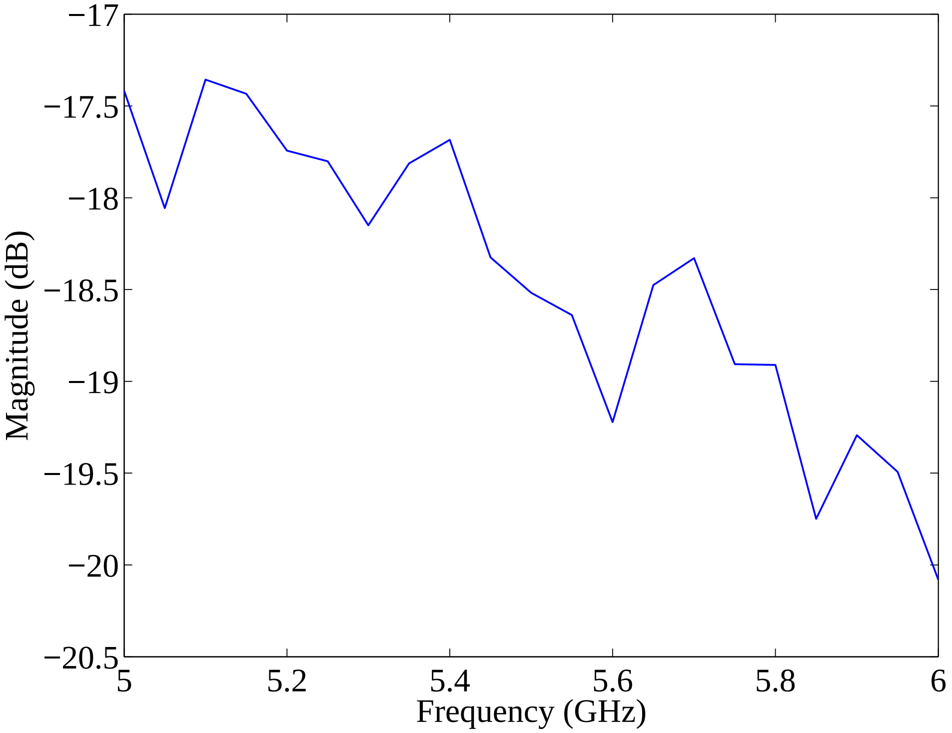

Figure B.3: Gain of the cables

B.2.2 Horn (Source) Antenna Gain

A calibration file for the horn antenna was supplied by Diamond Engineering. Figure B.4 shows the gain of the horn antenna over the desired frequency range. There is approximately a 1 dB difference between the maximum and minimum gain value.

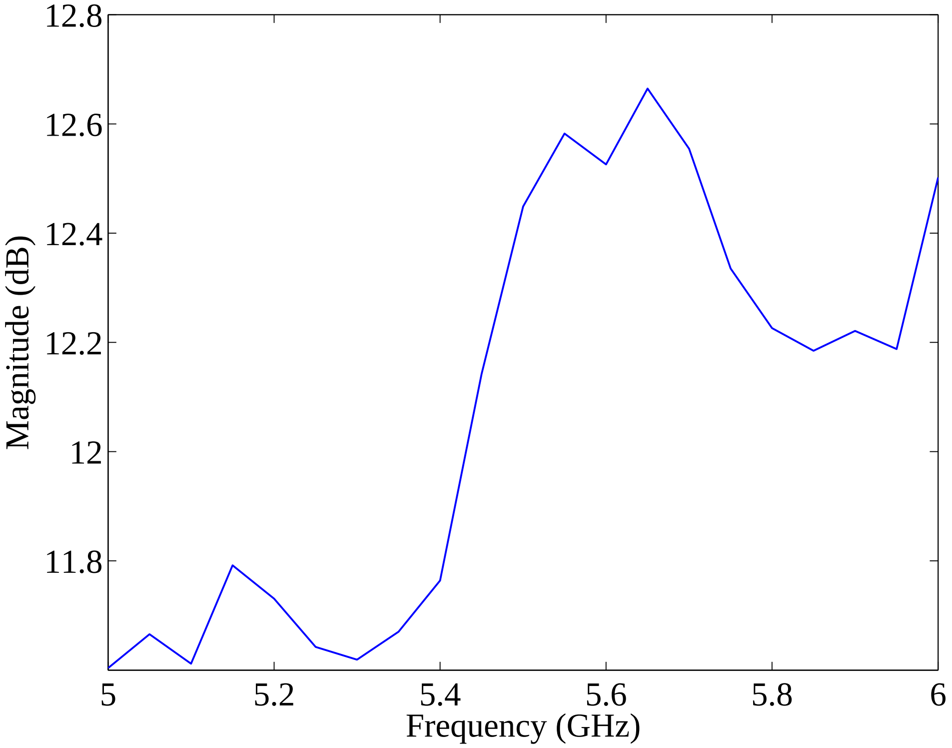

Figure B.4: Horn antenna gain

B.2.3 Path Gain

The Friis transmission equation is used to calculate the path gain. This calculation is very accurate for line of sight propagation with no obstructions and no reflections [1], and therefore is used for path gain inside the anechoic chamber. The Friis transmission equation presented in Equation B.4, where λ is the wavelength and d is the path length, was taken from [1], and can be found in many electromagnetics books.

$$G_{Path} = 10\log_{10}\left(\left(\frac{\lambda}{4\pi d}\right)^2\right) = 20\log_{10}\left(\frac{\lambda}{4\pi d}\right) \tag{B.4}$$

Using Equation B.4, with a path length $d = 2.87$ m, the path gain for the desired frequency range was calculated, see Figure B.5.

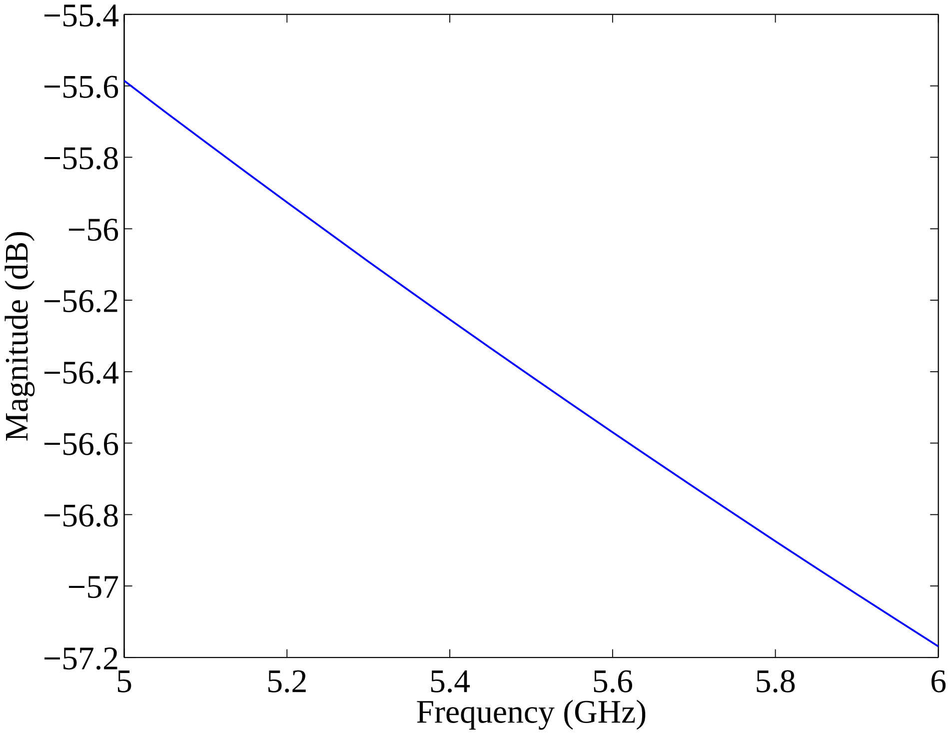

Figure B.5: Path gain

APPENDIX C

Transmission Line Theory

A transmission line can be designed and analyzed using equations presented in this appendix. While the first section discusses the transmission line design, the second section discusses the analysis associated with a given transmission line. Microstrip transmission line design entails calculating the width of a transmission line for a desired characteristic impedance, whereas transmission line analysis is used to calculate the characteristic impedance of a given transmission line. The equations presented were taken from [20], but they can be found in any microwave engineering and electromagnetics book.

Due to the presence of fringing fields, these equations are approximate expressions which have been developed by many researchers over the course of many years. Additionally, the parameters are calculated with piece-wise defined expressions based on the width to height ratio (w/h), where the width (w) corresponds to the width of the transmission line, and the height (h) corresponds to the height of the dielectric substrate above the ground plane.

C.1 Transmission Line Design

With the assumption that the transmission line conductor is infinitely thin, the width (w) of a transmission line can be calculated for a desired characteristic impedance (Z_0), given the height (h) and relative permittivity (ϵ_r) of the substrate material. Using Figure C.1 the approximate w/h ratio can be determined for a specific characteristic impedance given the permittivity of the substrate. If the approximate w/h ratio is less than or equal to two, use equations presented in Section C.1.1, and if the w/h ratio is greater than two, use the

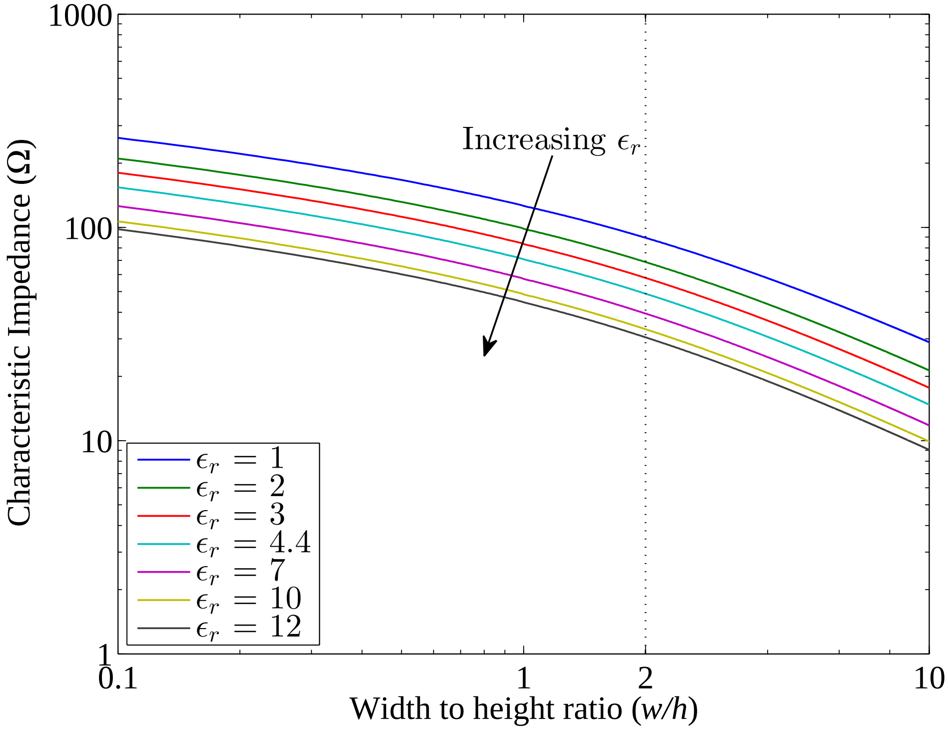

Figure C.1: Characteristic impedance as a function of the width to height ratio (w/h)

equations presented in Section C.1.2. For both cases, the wave impedance in free space (Z_f) is given by Equation C.1.

$$Z_f = \sqrt{\mu_0/\epsilon_0} \approx 376.8\Omega \tag{C.1}$$

C.1.1 Case One

If the approximate w/h ratio was determined to be less than or equal to two $(w/h \leq 2)$, from Figure C.1, then the transmission line width (w) can be determined with Equation C.2, where the factor A is given in Equation C.3.

$$w = h\frac{8e^{A}}{e^{2A} - 2} \tag{C.2}$$

$$A = 2\pi\frac{Z_0}{Z_f}\sqrt{\frac{\epsilon_r + 1}{2}} + \frac{\epsilon_r - 1}{\epsilon_r + 1}\left(0.23 + \frac{0.11}{\epsilon_r}\right) \tag{C.3}$$

C.1.2 Case Two

If the approximate w/h ratio was determined to be greater than two ($w/h > 2$), from Figure C.1, then the transmission line width (w) can be determined with Equation C.4, where the factor B is given in Equation C.5.

$$w = h\frac{2}{\pi}\left\{B - 1 - \ln\left(2B - 2\right) + \frac{\epsilon_r - 1}{2\epsilon_r}\left[\ln\left(B - 1\right) + 0.39 - \frac{0.61}{\epsilon_r}\right]\right\} \tag{C.4}$$

$$B = \frac{Z_f\pi}{2Z_0\sqrt{\epsilon_r}} \tag{C.5}$$

C.2 Transmission Line Analysis

With the assumption that the transmission line conductor thickness, t, and the substrate height, h, satisfy the relationship $t/h \ll 1$, then the analytical formulas to calculate the characteristic impedance of a transmission line only depend on the electromagnetic properties of the substrate (ϵ), the width of the transmission line (w), and the substrate height (h). If the w/h ratio is less than or equal to one, use the equations presented in Section C.2.1, and if the w/h ratio is greater than one, use the equations presented in Section C.2.2. The equations in both cases use the wave impedance in free space (Z_f) given in Equation C.1.

C.2.1 Case 1

For narrow microstrip transmission lines, $w/h < 1$, the characteristic impedance is calculated using Equation C.6, where the wave impedance in free space (Z_f) is given by Equation C.1 and the effective dielectric constant (ϵ_{reff}) is given by Equation C.7.

$$Z_0 = \frac{Z_f}{2\pi\sqrt{\epsilon_{\text{reff}}}} \ln\left(8\frac{h}{w} + \frac{w}{4h}\right) \tag{C.6}$$

$$\epsilon_{\text{reff}} = \frac{\epsilon_r + 1}{2} + \frac{\epsilon_r - 1}{2}\left[\left(1 + 12\frac{h}{w}\right)^{-\frac{1}{2}} + 0.04\left(1 - \frac{w}{h}\right)^2\right] \tag{C.7}$$

C.2.2 Case 2

For wide microstrip transmission lines, $w/h > 1$, the characteristic impedance is calculated using Equation C.8, where the wave impedance in free space (Z_f) is given by Equation C.1 and the effective dielectric constant (ϵ_{reff}) is given by Equation C.9.

$$Z_0 = \frac{Z_f}{\sqrt{\epsilon_{\text{reff}}}\left(1.393 + \frac{w}{h} + \frac{2}{3}\ln\left(\frac{w}{h} + 1.444\right)\right)} \tag{C.8}$$

$$\epsilon_{\text{reff}} = \frac{\epsilon_r + 1}{2} + \frac{\epsilon_r - 1}{2}\left(1 + 12\frac{h}{w}\right)^{-1/2} \tag{C.9}$$